

*NASA Contractor Report 198283*

*ICASE Report No. 96-12*

# ICASE

## COMPUTATIONAL STUDY OF CHAOTIC AND ORDERED SOLUTIONS OF THE KURAMOTO-SIVASHINSKY EQUATION

**Yiorgos S. Smyrlis  
Demetrios T. Papageorgiou**

**DISTRIBUTION STATEMENT A**

Approved for public release  
Distribution Unlimited

*NASA Contract No. NAS1-19480  
February 1996*

*Institute for Computer Applications in Science and Engineering  
NASA Langley Research Center  
Hampton, VA 23681-0001*

*Operated by Universities Space Research Association*



*National Aeronautics and  
Space Administration*

*Langley Research Center  
Hampton, Virginia 23681-0001*

*DTIC QUALITY INSPECTED*

**19960417 145**

# **Computational study of chaotic and ordered solutions of the Kuramoto-Sivashinsky equation**

*Yiorgos S. Smyrlis\**

Department of Mathematics & Statistics  
University of Cyprus  
Nicosia, Cyprus

*Demetrios T. Papageorgiou†*

Department of Mathematics &  
Center for Applied Mathematics & Statistics  
New Jersey Institute of Technology  
Newark, NJ 07102

## **Abstract**

We report the results of extensive numerical experiments on the Kuramoto-Sivashinsky equation in the strongly chaotic regime as the viscosity parameter is decreased and increasingly more linearly unstable modes enter the dynamics. General initial conditions are used and evolving states do not assume odd-parity. A large number of numerical experiments are employed in order to obtain quantitative characteristics of the dynamics. We report on different routes to chaos and provide numerical evidence and construction of strange attractors with self-similar characteristics. As the "viscosity" parameter decreases the dynamics becomes increasingly more complicated and chaotic. In particular it is found that regular behavior in the form of steady state or steady state traveling waves is supported amidst the time-dependent and irregular motions. We show that multimodal steady states emerge and are supported on decreasing windows in parameter space. In addition we invoke a self-similarity property of the equation, to show that these profiles are obtainable from global fixed point attractors of the Kuramoto-Sivashinsky equation at much larger values of the viscosity.

---

\*The work of Y.S. Smyrlis was supported by NATO Grant CRG 920097.

†The work of D.T. Papageorgiou was supported by the National Science Foundation Grant NSF-DMS-9003227 and by NATO Grant CRG 920097. Additional support was also provided by the National Aeronautics and Space Administration under NASA Contract No. NAS1-19480 while he was in residence at the Institute for Computer Applications in Science and Engineering (ICASE), NASA Langley Research Center, Hampton, VA 23681-0001.

# 1 Introduction

The Kuramoto-Sivashinsky equation is one of the simplest one-dimensional PDE's which exhibits complex dynamical behavior. As an evolution equation it arises in a number of applications including concentration waves and plasma physics ([4], [20], [21], [22]), flame propagation and reaction diffusion combustion dynamics ([30], [31]), free surface film-flows ([2], [14], [29]) and two-phase flows in cylindrical or plane geometries [7], [11], [25], [35], [36]. The equation can be written as

$$U_t + UU_x + U_{xx} + U_{xxxx} = 0, \quad x \in [-\frac{L}{2}, \frac{L}{2}]_{per}, \quad (1)$$

noting that the solution remains periodic of period  $L$  if the initial data are periodic.

Equation (1) can be normalized to  $2\pi$ -periodic domains by the transformations  $x_1 = \pi x/L$ ,  $U = \pi u/L$  and  $t_1 = \pi^2 t/L^2$ , which on dropping the subscripts 1 yields the scaled KS equation

$$\begin{aligned} u_t + uu_x + u_{xx} + \nu u_{xxxx} &= 0, \\ (x, t) &\in \mathbb{R}^1 \times \mathbb{R}^+, \\ u(x, t) &= u(x + 2\pi, t), \end{aligned} \quad (2)$$

where  $\nu = \frac{\pi^2}{L^2} > 0$  represents a dimensionless wavelength of  $u$ . Physically, then, the limit  $\nu \rightarrow 0$  corresponds to the waves in (2) becoming infinitely long. It is easily established by linearization of (2) that for a given  $\nu$  the first  $\text{mod}(\nu^{-\frac{1}{2}})$  Fourier modes are linearly unstable and grow exponentially. It is well-known, from numerical experiments for instance (see below), that solutions to (2) become increasingly irregular as  $\nu$  is decreased.

Without loss of generality the study of solutions with zero spatial mean is sufficient due to Galilean invariance. An analytical study of the KS equation was carried out by Nicolaenko et al. [24] (referred to as [NST]), where it is shown that if the initial data are in  $L^2$  and are of odd-parity (i.e. antisymmetric about  $x = 0$  for (1) or  $x = \pi$  for (2)), then the solutions remain in  $L^2$  for all time and there is a globally attracting set also bounded in  $L^2$ . The bound depends on the value of  $L$  or  $\nu$  and the estimate of [24] gives the following upper bound:

$$\limsup_{t \rightarrow \infty} \|u(\cdot, t)\|_2 \leq \text{const} \cdot \nu^{-3/2}. \quad (3)$$

The corresponding bound for (1) is  $O(L^{5/2})$ . Such bounds of the  $L^2$  norm are useful in determining estimates of the Hausdorff dimension,  $d_H$ , of the universal attractor. In fact working with equation (1), it has been shown by Temam [34], that if the bound for the  $L^2$  norm is  $O(L^\alpha)$  then  $d_H$  is proportional to  $L^{(7+2\alpha)/8}$  and so the [NST] result yields the estimate  $L^{13/8}$  for  $d_H$ ; we note that the conjectured best bound is  $O(L)$  but a proof is not available yet.

The analysis in [NST] was based on the odd-parity of the initial data. This restriction has been removed recently by several authors. Goodman [13] considers general smooth initial data and obtains a bound of the same form as (3). This bound is improved further, however, by Il'yashenko [17] and independently using a more classical approach by Collet et al. [5], and is

$$\limsup_{t \rightarrow \infty} \|u(\cdot, t)\|_2 \leq \text{const} \cdot \nu^{-13/10}. \quad (4)$$

Again the analogous bound for (1) is  $O(L^{8/5})$  improving the estimate of the Hausdorff dimension to  $L^{51/40}$  bringing it closer to the conjectured best bound. We note that the analysis in [5] and [17] applies also to odd-parity initial conditions and so is an improvement of the method in [NST].

Analyticity of the solution has also been proved by Collet et al. [6]. In fact, considering equation (1), the result proved is that for large  $t$ , the function  $U(x, t)$  is analytic in  $x$  in a strip of width

$\beta \geq \text{const} \cdot L^{-16/25}$  around the real axis, which in turn implies that the high frequency part of the spectrum has the form

$$|U_n(t)| \approx O(\exp(-\text{const} \cdot L^{-16/25} q|n|)), \quad (5)$$

where  $U_n(t)$  is the  $n$ th Fourier coefficient of  $U(x, t)$  and  $q = 2\pi/L$ . By a series of numerical experiments a much stronger result than (5) has been conjectured in [6], namely that there exists a  $\beta > 0$  independent of  $L$  such that the solutions of (1) satisfy

$$\lim_{t \rightarrow \infty} \sup \sum_{n \in \mathbb{Z}} |e^{\beta q|n|} U_n(t)|^2 \leq \text{const.}, \quad (6)$$

and the numerical work gives  $\beta \approx 3.50$ . These results are extremely useful in guiding our numerical work as is explained in Section 2.

There are several computational and analytical studies dealing with the construction of approximate inertial manifolds of KS. Kirby [19] develops a Galerkin approximation based on Sobolev eigenfunctions; Chen [3] constructs approximate inertial manifolds by broadening the gaps in the spectrum in order to obtain low dimensional behavior; Foias et al. [10] construct fully discrete nonlinear Galerkin schemes based on approximate inertial manifolds of KS; Robinson [28] uses the bounds of [5] and [17] to produce a new estimate of the dimension of the globally absorbing set of KS. Additional references may be found in these articles.

A significant amount of numerical work preceded the theoretical results outlined above. The numerical experiments revealed a wealth of interesting nonlinear phenomena and in particular highly complex dynamics including chaotic trajectories as the dissipation parameter  $\nu$  decreases. Earlier works include the computations of Cohen et al. [4], Sivashinsky and Michelson [32], Aimar [1], and Manneville [23]. Systematic explorations of phase space were carried out by Hyman and Nicolaenko [15] and Hyman et al. [16], Papageorgiou and Smyrlis [27], [33] and Coward et al. [7] who report on many features of the dynamics. Kevrekidis et al. [18] computed the bifurcation diagram for relatively large values of  $\nu$ , using a bifurcation algorithm. For smaller values of  $\nu$  unsteady phenomena set in; it was first found by Papageorgiou and Smyrlis [27] and also Smyrlis and Papageorgiou [33], that in the case of odd-parity initial conditions there is a period-doubling route to chaos. Extensive numerical solutions were employed to provide strong evidence that the route to chaos is according to the Feigenbaum scenario ([8], [9]); in addition the universal constants computed by Feigenbaum for one-dimensional nonlinear non-invertible maps, were computed from our numerical data with two digit accuracy. In the sequel we term chaotic dynamics just beyond the accumulation point, in parameter space, as Feigenbaum chaos.

In this article we present the results of extensive numerical computations for general initial conditions. Comparisons with previous studies (e.g. [15], [16], [18]) have been made where there is an overlap with full agreement. Our particular interest is in lower values of  $\nu$  where the dynamics gets increasingly complicated.

## 2 Numerical methods

### 2.1 Approximation of the solution

The assumption that the initial data is spatially periodic of period  $2\pi$ , allows us to represent the solution  $u(x, t)$  of the Kuramoto-Sivashinsky equation (from now on KS) as :

$$u(x, t) = \sum_{k \geq 1} (\alpha_k(t) \cos kx + \beta_k(t) \sin kx) + \alpha_0(t) \quad (7)$$

The conservative nature of KS implies that  $\alpha_0(t)$  remains constant, i.e.

$$\begin{aligned}\frac{d\alpha_0(t)}{dt} &= \frac{1}{2\pi} \frac{d}{dt} \int_0^{2\pi} u(x, t) dx = \frac{1}{2\pi} \int_0^{2\pi} u_t(x, t) dx \\ &= -\frac{1}{2\pi} \int_0^{2\pi} (uu_x + u_{xx} + \nu u_{xxxx}) dx = 0.\end{aligned}$$

One could easily observe that whenever  $u(x, t)$  is a solution then so is  $u(x - ct, t) + c$ , which allows us to assume  $\alpha_0(t) = 0$  for simplicity. Replacing  $u(x, t)$  by its Fourier representation in the PDE we obtain

$$\begin{aligned}u_t + uu_x + u_{xx} + \nu u_{xxxx} &= \\ = \sum_{k \geq 1} (\alpha'_k - (k^2 - \nu k^4)\alpha_k - A_k) \cos kx + (\beta'_k - (k^2 - \nu k^4)\beta_k - B_k) \sin kx\end{aligned}$$

where

$$A_k = -\frac{k}{2} \sum_{m+n=k} \alpha_m \beta_n + \frac{k}{2} \sum_{m-n=k} (\alpha_m \beta_n - \alpha_n \beta_m) \quad (8)$$

and

$$B_k = \frac{k}{4} \sum_{m+n=k} (\alpha_m \alpha_n - \beta_m \beta_n) + \frac{k}{2} \sum_{m-n=k} (\alpha_m \alpha_n + \beta_m \beta_n) \quad (9)$$

Thus finally KS equation becomes equivalent to an infinite dimensional system of ODEs :

$$\alpha'_k = \lambda_k \alpha_k + A_k \quad (10)$$

$$\beta'_k = \lambda_k \beta_k + B_k \quad (11)$$

where  $k \in \mathbb{N}$  and  $\lambda_k = k^2 - \nu k^4$  with

$$A_k = A_k(\alpha_1, \alpha_2, \dots, \beta_1, \beta_2, \dots) \quad \text{and} \quad B_k = B_k(\alpha_1, \alpha_2, \dots, \beta_1, \beta_2, \dots)$$

In the case of the *Generalized Kuramoto-Sivashinsky equation*

$$u_t + uu_x + u_{xx} + \nu u_{xxxx} + \mathcal{D}u = 0 \quad (12)$$

where  $\mathcal{D}$  is a dispersive kernel, see Papageorgiou et al [25], the resulting infinite dimensional system of ODEs is quite similar

$$\alpha'_k = \lambda_k \alpha_k + \delta \beta_k + A_k \quad (13)$$

$$\beta'_k = \lambda_k \beta_k - \delta \alpha_k + B_k \quad (14)$$

where  $\delta$  is defined by

$$(\mathcal{D}u)(k) = i\delta \hat{u}(k) \quad (15)$$

It is already established by Il'yashenko [17], Collet et al [5], Goodman [13], that all the spatial Sobolev norms of the solution of KS equation for arbitrary initial conditions, remain bounded for all times, which implies that

$$\omega_k = \lim_{t \rightarrow +\infty} \sup |\alpha_k|^2 + |\beta_k|^2|^{1/2}$$

decays faster than any algebraic rate. Collet et al. [6] have already proved that the decay is exponential. Furthermore they present numerical evidence to support a conjecture that the number of determining Fourier coefficients is proportional to  $\nu^{-1/2}$ .

Such numerical evidence justifies approximation of the solution of the KS by truncation of higher frequencies. The size of the truncation can be determined by the Collet et al. [6] numerical study of the decay rate of the Fourier coefficients, but a first estimate of this is obtainable from the argument that follows. The KS equation in Fourier space can be written as :

$$\frac{d}{dt}\hat{u}(k, t) = \lambda_k \hat{u}(k, t) - (\hat{u}\hat{u}_x)(k, t) \quad (16)$$

or

$$\frac{d}{dt}\hat{u}(k, t) = \lambda_k \hat{u}(k, t) - ik\left(\frac{1}{2}\hat{u}^2\right)(k, t) \quad (17)$$

We also have :

Fact : If  $\mu$  is positive and  $f(t)$  is in  $L^\infty[0, +\infty)$  then the solution of  $x' + \mu x = f(t)$  satisfies:

$$\lim_{t \rightarrow +\infty} \sup |x(t)| \leq \frac{1}{\mu} \|f\|_\infty \quad (18)$$

Using the above result in combination with (17), we observe that, if we had, even a rather rough estimate of the size of  $u$  and its norms, we could obtain an idea of the number of Fourier coefficients with *significant numerical* contribution to the approximate solution of the KS equation.

Having used various numerical schemes, we obtained sufficiently good estimates of the size of  $u$ , as well as of  $u^2$ ,  $uu_x$  and of  $|u|_{L^2}$ . Thus we subsequently obtained an estimate of the number of numerically significant Fourier coefficients. It should be mentioned here that the existing analytical results alone can not be of much practical value in determining the truncation size.

Currently we use a finite difference scheme of variable time step to integrate the truncated system of ODEs

$$\alpha'_k = \lambda_k \alpha_k + A_k^N(\alpha_1, \alpha_2, \dots, \alpha_N, \beta_1, \beta_2, \dots, \beta_N) \quad (19)$$

$$\beta'_k = \lambda_k \beta_k + B_k^N(\alpha_1, \alpha_2, \dots, \alpha_N, \beta_1, \beta_2, \dots, \beta_N) \quad (20)$$

where  $k = 1, 2, \dots, N$  and

$$A_k^N = -\frac{k}{2} \sum_{m=1}^{k-1} \alpha_m \beta_{k-m} + \frac{k}{2} \sum_{m=1}^{N-k} (\alpha_m \beta_{m+k} - \alpha_{m+k} \beta_m) \quad (21)$$

$$B_k^N = \frac{k}{4} \sum_{m=1}^{k-1} (\alpha_m \alpha_{k-m} - \beta_m \beta_{k-m}) + \frac{k}{2} \sum_{m=1}^{N-k} (\alpha_m \alpha_{m+k} + \beta_m \beta_{m+k}) \quad (22)$$

Our scheme turns out to be extremely stable due to the form of the linear part of the right hand side of the system. We emphasize that even though  $\lambda_k$  is bounded from above, with a mild upper bound namely

$$\lambda_k \leq \frac{1}{4\nu},$$

for all  $k \in \mathbb{N}$ , it could have a negative lower bound very large in absolute in our truncated system. For example, if  $N = 32$ ,  $\nu = .01$  then  $\lambda_N \approx -9.5 \times 10^3$ . Thus if  $\Delta t$  is such that

$$|l_N|\Delta t = O(1)$$

then the relative local numerical error for  $\alpha_N, \beta_N$  is also  $O(1)$ , since at each time step the linear semigroup multiplies  $\alpha_N, \beta_N$  by  $\exp(l_N\Delta t)$ . We should also note here that in the nonlinear part of the system of ODEs corresponding to high frequencies in our truncated system, i.e.,  $A_k^N, B_k^N$ , most of the contribution comes from the low frequency coefficients. This implies that higher frequency coefficients are *slaved* by the low frequency ones due to the scheme; this is a distinguishing feature of dissipative infinite dimensional dynamical systems and is thus inevitable. Still we wish to allow the high frequencies as much freedom as possible in order to enable potential individual behavior. In achieving this we incorporate a modification suitable for stiff systems of ODEs. Stiffness is caused here by the big variation of the values of  $\lambda_k$  and thus the time step in our modified scheme varies according to the size of  $\lambda_k$ . Nevertheless the relative local error in every individual term also varies, in our scheme, according to its contribution to the solution.

Altogether the local numerical error, due to the approximation of the solution of the system of ODEs, is reduced to be insignificant compared to the one caused by the truncation alone. It should be clarified at this point that even with coarser time step subdivisions than the ones in current use, the relative local error to the solution profile due to the high frequencies is satisfactory. High order accuracy, i.e. the local relative error being kept below the level of  $10^{-6}$ , is employed only for the sake of studying high order frequencies and their long time influence on the nature of the global attractor.

## 2.2 Numerical Experiments

We have carried out a very large number of numerical experiments, testing more than 800 values of the dissipation parameter  $\nu$  ranging from<sup>†</sup>  $\nu = .99999999$  to  $\nu = .002$ . In representative values of our dissipative parameter  $\nu$  we carried out several runs to make sure that the behavior of the attractor corresponding to that  $\nu$  does not change with more Fourier coefficients of finer time step. This is necessary since our major concern is not just the local error but faithful reproduction of the long time behavior. The size of the truncation ranged from  $N = 4$  to  $N = 512$  making computation in the latter case rather slow. Most important of all is that many cases had to be followed for very long time in order to achieve convergence to the corresponding attractor and/or to accurately classify the attractor. For example in the case  $\nu = .1212267996068$ , the attractor is

---

<sup>†</sup>If  $\nu \geq 1$  then

$$\lim_{t \rightarrow +\infty} u(x, t) = \bar{u}_0 = \frac{1}{2\pi} \int_0^{2\pi} u_0(x) dx, \quad (23)$$

since KS equation implies that

$$\frac{1}{2} \frac{d}{dt} |u(\cdot, t)|_2^2 = |u_x(\cdot, t)|_2^2 - \nu |u_{xx}(\cdot, t)|_2^2$$

and for  $u \in L^2[0, 2\pi]$ ,  $2\pi$ -periodic, with  $\int_0^{2\pi} u(x) dx = 0$  we have the following inequalities:

$$|u|_2 \leq |u_x|_2 \leq |u_{xx}|_2$$

On the other hand if  $\nu \leq 0$  the problem is ill-posed.

periodic with  $2^{14}$  distinct maxima and as many minima in the  $L^2$  norm as a function of time. This particular value of  $\nu$  follows previous ones corresponding to 13 period doubling bifurcations. The period is estimated to be  $T \approx 25573$ , which corresponds to approximately  $5.1 \times 10^7$  time steps and each step corresponding to substeps. Satisfactory convergence to the periodic attractor occurred after  $10^9$  time steps.

In representative cases, of different values of  $\nu$ , we have used our method to estimate the error caused by the truncation. The relative error, with respect to the  $L^2$  and  $H^1$  norms ranged from  $10^{-6}$  to numerically insignificant. Though  $10^{-6}$  might look big, we should point out that our study's major target was not to run the most accurate algorithm - which we did in selected cases. Instead it was to carry out many and long runs, and keep sufficient accuracy, in order to reproduce the nature of the corresponding attractor. Classification of the nature of the attractors at each different value of  $\nu$  made it possible to determine the windows in the parameter  $\nu$  space. Most of the runs had to be carried out in order to accurately determine the limits of the windows of  $\nu$ , and furthermore determine whether the transition between the two kinds of attractors was smooth or not. A case of a smooth transition is a bifurcation; A period-doubling is one such as well as a case of eigenvalues bifurcations of the Jacobian of the flux of our dynamical system which cause transition from stationary/traveling attractors to periodic or chaotic ones. A non-smooth transition is a case when we have for a  $\nu$ -interval,  $[\nu_1, \nu_2]$  say, coexistence of two or more invariant locally attracting sets. While one of them was attracting *most* of the initial data, as  $\nu$  varies, another one becomes suddenly more likely to attract most initial data. For example, in the case of  $\nu = .232$ , we have coexistence of a unimodal traveling attractor and of one with periodically appearing homoclinic bursts. The second one is *more attracting*. Even though the exact bifurcation values of  $\nu$  depend on the accuracy of the numerical scheme, the nature of the bifurcation does not depend on the accuracy provided that the method is of sufficient accuracy since the system has finite degrees of freedom. This observation forces us to use higher accuracy when we seek better approximation of the bifurcation values of  $\nu$ .

### 2.3 Characterization of the attractors

As  $\nu$  varies the long time behavior of the solution does also, in some cases smoothly and in others not. Different values of  $\nu$  correspond to stationary (unimodal, bimodal, trimodal,...), traveling, periodic and chaotic attractors. Stationary attractors are easy to observe, and their stability can be studied with standard methods. It suffices to check the eigenvalues of the Jacobian of the truncated system at the stationary profile. Similarly in the case of traveling profiles, where one could easily determine its speed of propagation :

$$c = \frac{1}{\Delta t} \text{Arg}\left(\frac{\alpha_1 \bar{\alpha}_1 + \beta_1 \bar{\beta}_1}{\alpha_1^2 + \beta_1^2}, \frac{\alpha_1 \bar{\beta}_1 - \beta_1 \bar{\alpha}_1}{\alpha_1^2 + \beta_1^2}\right) + O(\Delta t^2) \quad (24)$$

where

$$(\alpha_1, \beta_1) = (\alpha_1(t - \Delta t), \beta_1(t - \Delta t))$$

$$(\bar{\alpha}_1, \bar{\beta}_1) = (\alpha_1(t + \Delta t), \beta_1(t + \Delta t))$$

In the case of periodic attractors more sophisticated numerical methods are required for their quantification. First suspicion of a periodic attractor comes from the energy versus time plot -

$E(t) = |u(t, \cdot)|_{L^2}$ . The evidence becomes more convincing once we obtain the phase plane of the energy plots - i.e.  $E(t)$  versus  $dE(t)/dt$ , where the values of  $dE(t)/dt$  are accurately obtainable using a suitable interpolation of several points  $(t_k, E(t_k))$ . Periodic attractors correspond to closed phase curves and the number of minima/maxima is the number of the points where the phase curves intersect the  $E$ -axis, i.e.  $dE(t)/dt = 0$  with  $d^2E(t)/dt^2 > 0$  or  $< 0$  respectively.

Nevertheless we wish to have more accurate quantitative data such as the exact period as well as the exact values of the local extrema, in order to accurately determine period doubling bifurcations and study the potential fractal nature of the return map<sup>§</sup> of the extrema. In order to achieve that, we have used a method of calculation of the extrema by an optimized polynomial interpolation over a sufficiently large number of points  $(t_k, E(t_k))$ . The polynomial of the interpolation is obtained by a suitably weighted least squares method over consecutive points, many more than the degree of the polynomial sought for. Weights in the least squares approximation, reduce the effects of higher order polynomial terms and the round-off error caused by the computation of the quantity used in the interpolation. It is of critical importance that all points of the interpolation lie in the convex or concave region, when we look for minima or maxima respectively. This method, in the case of test functions, gave us accuracy higher than the machine precision, nevertheless, as it could be shown analytically, the precision in the estimation of local extrema, depend on the time step and the degree of the interpolation polynomial. Weights are introduced to make the points which are closer to the local extremum have a higher contribution to the interpolation.

The original motive in developing the interpolation algorithm was to accurately determine the period doubling bifurcations and establish the appearance of the Feigenbaum universal constants. (See Smyrlis and Papageorgiou [33].) This method turned out to be extremely helpful in determining features such as the fractal nature of attractors, by detecting such behavior in the return map of the energy minima, for example. Most successfully it has enabled us to detect and classify the quasiperiodicity of attractors. We should mention here that the same conclusions, concerning periodic attractors are also obtainable if instead of the  $L^2$  norm and its extrema we had used for their detection, other quantities such as the  $H^1$  norm and the Fourier coefficients. However there is an exception here, the case of traveling/periodic attractors, where instead of

$$u(x, t + T) = u(x, t) \quad \text{for all } (x, t) \in \mathbb{R} \times \mathbb{R}^+$$

we have

$$u(x, t + T) = u(x - cT, t) \quad \text{for some } c \in \mathbb{R}$$

Thus  $E(t)$  has period  $T$ , but  $\hat{u}(k, t)$  is in general a quasiperiodic function unless  $cT/2\pi$  is a rational number. Fourier coefficients being quasiperiodic produce very beautiful pictures -  $\alpha_k(t)$  versus  $\beta_k(t)$ . The speed of propagation and period could also be accurately estimated using a suitable interpolation.

In the classification of chaotic attractors and transitions to chaos scenarios, then, the extrema of  $E(t)$  and their return maps played the key role. We should mention here that if  $f(t)$  is a quasiperiodic function, for example

$$f(t) = \cos t + \cos(\sqrt{2}t),$$

then, although there is not much to observe in the graph, one could observe a lot in the *return map*. If  $(m_k)_{k \in \mathbb{N}}$  is the sequence of the local minima, in the order they appear for  $t \geq 0$ , then their

---

<sup>§</sup>Let  $a_n$ ,  $n \in \mathbb{N}$  be a sequence of real numbers, then the set of points  $(a_n, a_{n+1})$ ,  $n \in \mathbb{N}$ , which is a subset of  $\mathbb{R}^2$ , is called the *Return Map* of  $(a_n)_{n \in \mathbb{N}}$ . In the case of a function  $f : [0, \infty] \rightarrow \mathbb{R}$  the return map of  $f$  is the return map of the sequence of the local minima (or maxima or extrema) of  $f$ .

return map, lies on a closed curve. In general if  $f_1(t)$ ,  $f_2(t)$  are periodic functions with irrational frequency ratios, then the return map of  $f(t) = f_1(t) + f_2(t)$  lies on one or more lines. This is generalized to three or more irrational frequencies.

Visualization of the return map of the local minima (or maxima) of the energy (or other quantities such us the  $H^1$  norm which magnifies the contribution of high frequencies) enables us to classify the attractors, not only in the quasiperiodic case, but also in more complicated chaotic ones.

In certain cases the return map plot has a fractal nature. Foliations are observable when one plots successive magnifications of the graphs. We are in the process of estimating numerically the Hausdorff dimension of the graph corresponding to the return map in order to establish the rate of growth of the Hausdorff dimension as  $\nu$  decreases, particularly in those chaotic cases where there is no recognizable pattern. In such studies it is imperative that the local extrema are computed with a high accuracy, in particular if magnifications in the return map of several orders of magnitude are to be carried out.

### 3 Numerical results

#### 3.1 Dynamics for “large” $\nu$ : $0.09 < \nu < 1$

For values of  $\nu$  larger than about 0.1 a fairly complete picture of the dynamics has been given by numerous authors ([15], [16], [18]). Steady state or traveling waves, including their bifurcation diagrams are computable by well-developed bifurcation algorithms, see for example ([18]). Our interest is on the spatio-temporal evolution in chaotic attractors which led to the development of the accurate code tracking the time evolution of solutions, described in Section 2. For completeness, however, and to set the stage for the results that follow we give a brief description of the dynamics corresponding to “large”  $\nu$ . We note that as  $\nu$  decreases computed attractors are not necessarily global ones; our numerical results are based on large time solutions of general initial value problems and the numerical solutions given here belong to the most strongly attracting ones in the sense that they are reproduced by fairly different initial conditions (e.g. a sinusoidal initial condition or one having a white noise spectrum).

A schematic of the dominant attractors in this range is given in Figure 1. The interval  $\nu \geq 1$  is not included in Figure 1 since it is trivial in the sense that a uniform steady state is achieved here which is equal to the spatial mean of the initial data. The figure is drawn to scale in order to give the relative sizes of attractors. The letters A-F are used to identify the different intervals which are briefly described below. According to extensive computations, there is an interval (.12116, .1212267996064) which cannot be distinguished on Figure 1 due to its small size - we call this interval  $E_1$  and describe it below.

Interval A:  $0.307602 \leq \nu < 1$ .

For  $0.30765 < \nu < 1$  solutions get attracted to a  $2\pi$ -periodic steady state (unimodal fixed point). The energy, or the spatial  $L^2$ -norm of the solution, defined as  $E(t) = \int_0^{2\pi} u^2(x, t) dx$  increases as a function of  $\nu$  in this interval and attains a maximum at  $\nu \approx 0.59094$ .

Interval B:  $0.232491 \leq \nu \leq 0.307601$ .

For  $0.232491 < \nu \leq 0.307601$  a  $2\pi$ -periodic (unimodal) steady-state traveling wave is found - the wavespeeds increase monotonically from zero near the upper edge of the window to approximately 0.956 at  $\nu = 0.232491$ .

Interval C:  $0.17735 \leq \nu \leq 0.23249$ .

A bifurcation occurs just below  $\nu = 0.232491$ , and in the range  $0.17735 \leq \nu \leq 0.23249$  periodic homoclinic bursts (PHB) emerge as the most attracting states. The PHB solutions found in this window have  $L^2$ -norms which are constant except for periodically occurring homoclinic bursts. The time intervals between bursts vary from approximately 21 – 30 time units for  $\nu$  between 0.23249 and 0.2, and then increase dramatically as  $\nu$  decreases further; for example the time between bursts for  $\nu = 0.179, 0.178, 0.1775, 0.1774, 0.17735$  are approximately 200, 450, 1700, 4500 and 18000 time units respectively.

Representative results are given in Figures 2 and 3 for  $\nu = 0.2$ . Figure 2 shows the evolution of  $E(t)$  after the solution has settled into an attractor - a range between 750 and 1000 time units is shown. The energy is constant with homoclinic bursts occurring at approximately every 30 time units. The phase plane of  $E(t)$  provides strong evidence that the bursts are periodic. The solution spends most of its time at the rightmost point in the phase plane diagram and every 30 time units it loops around in less than 5 time units, with the process repeating periodically. The profile between bursts is steady for 30 time units and is in fact a bimodal fixed point, that is only even Fourier modes are non-zero. It has been confirmed that the bimodal profile during bursts is obtainable from the unimodal global fixed point attractor at  $\nu = 0.8$  by use of the property (26) discussed in Section 2. We can surmise, therefore, that the bimodal fixed point attractor is unstable and overlaps with a time-periodic attractor.

The evolution of  $E(t)$  does not provide details about individual Fourier coefficients since it is an integral quantity. The time history of the first two harmonics is given in Figure 3. The coefficients of  $\cos(x)$ ,  $\sin(x)$  and  $\cos(2x)$ ,  $\sin(2x)$  are plotted on the same scale so that their evolution can be followed concurrently. It is evident from the primary Fourier mode plots that the amplitudes are zero except during bursts which appear as sharp peaks. The peaks alternate from small size to larger size during each burst; there also seems to be an energy exchange between the two amplitudes in that during each burst the  $\cos(x)$  and  $\sin(x)$  amplitudes attain alternatively large and small peaks. The sign of individual amplitudes during bursts does not appear to have a recognizable pattern but seems to be random.

The situation is much more regular for the 2nd Fourier mode. The time evolution of the amplitudes of  $\cos(2x)$  and  $\sin(2x)$  are now in phase with bursts appearing as sharp jumps connecting equal but opposite steady states. Similar results persist for higher modes, the main difference being a marked decrease in amplitude.

Interval D:  $0.131815 \leq \nu \leq 0.1773$ .

The time increase between bursts heralds the appearance of a new fixed point attractor. It is found that in the range  $0.131815 \leq \nu \leq 0.1773$  solutions get attracted to bimodal steady states, i.e.  $\pi$ -periodic stationary profiles. According to the property (26) these solutions are obtainable from the unimodal solutions in the subinterval  $[0.5272, 0.7092]$  of  $A$  by choosing  $\rho = 2$ .

Intervals E,  $E_1$ :  $0.1212267996068 \leq \nu \leq 0.13181$ , and  $E_2$ :  $0.12116 \leq \nu \leq 0.1212267996064$ .

The bimodal steady states loose stability and a time periodic attractor is entered. The energy  $E(t)$  has an approximate period of 0.93862 time units at the beginning of the window,  $\nu = 0.13181$ . The period increases monotonically as  $\nu$  is decreased and the first period doubling takes place in the interval  $.12175 < \nu < .121752$ . This pattern is repeated, i.e. a monotonic increase in the period and then a period doubling, and the following eleven successive period doublings were found in each of the open intervals  $(.1213145, .121315)$ ,  $(.12124493, .12124495)$ ,  $(.12123065, .1212307)$ ,  $(.12122762, .12122775)$ ,  $(.121226975, .12122698)$ ,  $(.121226835, .12122684)$ ,  $(.121226805, .121226808)$ ,

(.1212268012, .1212268014), (.1212267998, .1212268), (.12122679968, .1212267997) and (.121226799622, .121226799625). The period by the twelfth period doubling is  $T \approx 12780$  time units. Figure 4 shows the phase planes of the energy for representative cases capturing the first five period-doublings. The values of  $\nu$  are given on the Figure as well as the number of minima of the energy - there are  $2^p$  minima where  $p$  is the number of period doublings that have taken place. It has been confirmed, but is not included here, that the cascade follows the Feigenbaum scenario ([8], [9]) with  $\nu$ -intervals between successive period doublings decreasing geometrically by a universal factor  $\delta = 4.6692016 \dots$ . The data analysis and methods used are identical to those of Papageorgiou and Smyrlis [27] and Smyrlis and Papageorgiou [33] who considered odd-parity solutions of the KS equation. The second Feigenbaum universal constant which pertains to the geometry of the attractor is also accurately supported by those results. By analogy with the theory of non-invertible one-dimensional maps, coupled with the numerical evidence given here, it is reasonable to assume that an accumulation point exists,  $\nu_0$  say, below which the solution is chaotic; this of course is hard to prove since we are dealing with differential systems of large dimensions (24 coupled equations are used in this window).

After extensive computations we are able to identify an interval  $E_1 = [0.12116, 0.1212267996064]$  which we describe as supporting Feigenbaum chaos. Evidence for this comes from the study of return maps of the energy minima (see Section 2 for a description of the data analysis tools used here) which give “strange attractors” with as many as  $2^{13}$  pieces at the beginning of interval  $E_1$ . The number of pieces decrease and when  $\nu = 0.12118$  the attractor consists of only one piece. A picture of a strange attractor constructed from the return map, is given in Figure 5(i)-(vii) which corresponds to  $\nu = 0.12122679907$ . The return map of a large number of energy minima beyond transient behavior is shown in Figure 5(i). There are 32,034 points in this plot and each point is represented by a dot. The points lie on a regular looking object and since each point gets mapped to another point in the plot by the action of the dynamical system, the pieces traced out mimic the analogous one-dimensional non-invertible map representation of the flow; the equivalent plot for the logistic map would trace out parts of a quadratic function. Interestingly, Figure 5(i) resembles the quadratic map but the differences have not been quantified. The similarity property of strange attractors is however exhibited in Figure 5. Starting from Figure 5(i), successive enlargements are made of the pieces of the attractor which are marked by the letter ‘e’. The scale of the enlargement can be followed by noting the horizontal scale of successive diagrams. The first enlargement, Figure 5(ii), is of what appear as two pieces in 5(i) near the minimum of the plot. On enlargement a picture which is clearly similar to the complete attractor in 5(i) emerges. The two pieces near ‘e’ in 5(ii) are enlarged to give 5(iii); again similarity with the previous plots is remarkable considering that an amplification of approximately a factor of 50 has taken place. The one piece near ‘e’ in 5(iii) is now enlarged to give the three clusters in 5(iv). The rightmost marked piece is enlarged to give 5(v) and its rightmost piece is enlarged to give 5(vi). Finally an enlargement of the leftmost marked cluster of 5(vi) gives the final plot Figure 5(vii) which contains just four points. The successive plots 5(iv)-(vii) provide additional strong evidence of the self-similarity of the attractor. We note that such conclusions are only possible if a large and accurate data base is available - for instance in going from Figure 5(i) to Figure 5(vii), an amplification factor of approximately  $3 \times 10^6$  has taken place along the horizontal axis. In the absence of a large and accurate data set of minima (see Section 2 for the interpolation algorithms), the number of return map “iterations” which produce the strange attractor would be inadequate for sufficient levels of enlargement that exhibit self-similarity. In addition loss of accuracy in the minima estimation would produce a noisy data set which is of little value in exhibiting self-similarity.

Interval F:  $0.09051 \leq \nu \leq 0.121155$ .

Near the upper edge of this window,  $0.121155 \leq \nu \leq 0.12105$ , solutions are attracted to homoclinic bursts, with the bursts being chaotic but with a low dimensional attractor. The bursts are spaced apart at roughly equal times and in between them the profile is bimodal and is obtainable from the equivalent unimodal steady state in interval  $A$  according to the self-similar property (26). Typical results are given for  $\nu = 0.12115$ . The homoclinic bursting is shown in the evolution of the energy and its corresponding phase-plane, Figures 6; the phase-plane indicates the non-periodicity of the bursts. It has been confirmed that the profile in between bursts is given by  $u(x; 0.12115) = 2U(2x; 0.4846)$  where  $U(y; \nu)$ ,  $0 \leq y \leq 2\pi$  is the steady-state profile in interval  $A$ . Further information about the chaotic bursts is given in Figures 7(a)-(b). Figure 7(a) gives the evolution with time of the critical points of  $E(t)$ , that is its local maxima and local minima. For a given time interval, there is a discrete set of energy maxima and minima and each of these is represented by a dot in the plot. The longer and relatively regularly spaced gaps with no points in the plot denote time intervals between bursts while darker segments correspond to the bursts. The irregularity of the positioning of the points indicates the chaotic aspect of the bursts and this can be seen more clearly in the return map of the energy minima in Figure 7(b) which suggests a strange attractor with foliations. The bimodal steady state in-between bursts is at the point  $(10.7415876, 10.7415876)$  on the return map diagram, which is marked with an open circle. Successive enlargements of the attractor are given in Figure 8(i)-(vi). Again the point corresponding to the inter-bursting bimodal steady state is marked with an open circle and five successive enlargements are made in its neighborhood. The similarity of the attractor is discernible, particularly if we note the horizontal extent of the attractor given in each plot in Figures (ii)-(vi); the horizontal extents are approximately 0.6, 0.15, 0.011, 0.001 and 0.000005 for Figures 8(ii)-(vi) respectively. An enlargement of the order  $10^5$  has taken place in going from Figure 8(ii) to Figure 8(vi) and the positioning of the dots, that is the geometry of the attractor, is remarkably similar; from a numerical point of view, we note that such details can only be captured if the energy minima are computed accurately to at least seven decimal places - this is another reason for the high order interpolation schemes used in constructing the minima from a set of energy values at discrete time intervals no smaller than the time-step of the integrator.

As the value of  $\nu$  is decreased below approximately 0.121045 the homoclinic bursts take place more regularly in time and they are almost periodic. A more careful scrutiny of the data from the representative case  $\nu = 0.1$  reveals that the flow is chaotic, and the bursting phenomenon has a low dimensional attractor. Once again the unstable quiescent states between bursts give profiles which are bimodal and given by  $u(x; 0.1) = 2U(2x; 0.4)$ . A plot of  $E(t)$  together with a magnification of a burst is shown in Figure 9. The bursts are almost periodic and take place every 33 time units, approximately; the energy phase-plane has been shown not to be a closed curve of index 2 as in the homoclinic burst solutions found in interval  $C$  described above. Figure 10 shows the return map obtained from the energy minima. The point marked P corresponds to the steady state in between bursts and as the magnification shows, the attractor in the neighborhood of this fixed point consists mainly of two lines meeting at an angle smaller than  $\pi/2$ . Additional information about the bursting is given in Figure 11. The Fourier amplitudes of the first four modes are plotted against time, that is we plot  $\sqrt{a_i^2 + b_i^2}$  for  $i = 1, 4$  where  $u(x, t) = \sum_{n=1}^N (a_n \cos(nx) + b_n \sin(nx))$  is the Fourier-Galerkin representation of the solution. In between bursts, only the even modes are non-zero and as seen from the plots the amplitude of the fourth mode is smaller than that of the second one. During a burst, however, the even modes loose energy to the odd modes as can be seen clearly from the Figure; the amplitude of even modes always decreases (except right at the end of the burst) and at the same time the amplitudes of odd modes become non-zero for the

duration of the burst but vanish again after the homoclinic burst is finished. This behavior is very characteristic of the global energy transfer mechanism present in the KS equation.

### 3.2 Dynamics for lower values of $\nu$ : $\nu < 0.09$ .

As  $\nu$  decreases the dynamics become more complicated. A larger number of determining modes is required and co-existence of attractors is more likely. From a numerical viewpoint the computations become more expensive and accuracy criteria more stringent.

A large number of numerical experiments have been carried out over several years and a summary of the attractors is given in Figure 12. The Figure represents the  $\nu$ -line (not drawn to scale) along with the most strongly attracting large time solutions found by us; note that the various attractors given in Figure 12 are not necessarily global ones but the window boundaries given delineate the regions where an attractor loses stability. The type of attractor was determined by applying the data analysis described earlier.

In interval  $E$  described earlier, we provided evidence of a period-doubling route to chaos, and also a route to chaos through homoclinic bursting as in interval  $F$  above. A third route to chaos is via a quasi-periodic attractor and this route is supported by the first three windows in Figure 12. A time periodic attractor loses stability to a quasi-periodic one at  $\nu = 0.087679$  and there is transition to chaos below  $\nu = 0.087023$ . It is quite hard to discern the difference between a chaotic attractor and a quasi-periodic one by inspection of the signal of  $E(t)$ . The return map is a valuable tool in doing this, since the return map (of the energy minima for instance) of a quasi periodic attractor consists of lines with no foliations; an analogy is the return map obtained from a Poincaré section of motion on a torus, in which case it is a circle whose perimeter becomes dense as the iterations increase. In the chaotic regime, the return map contains foldings and self-similarity as exhibited in several examples earlier. This type of chaotic motion is differentiated from what we term as unrecognizable chaos in that the tools employed by us to analyze the dynamics, yield information about the structure of the attractor.

As can be seen from Figure 12, among the regions of different unsteady and complicated spatio-temporal motions there emerge stable fixed point attractors with increasingly higher modal behavior, i.e. with shorter periods. In Figure 13 we give a summary of the computed attractors so far, as  $\nu$  decreases to approximately 0.006. The numbers on the figure denote the modal form of the solution, for example 3M is a trimodal attractor with the only non-zero Fourier coefficients being multiples of three. As already noted in the Appendix, one can construct steady states of increasingly shorter periods (i.e. higher modal behavior) by application of the similarity property (26). This construction does not imply stability but our numerical results produced by solving initial value problems, show that such fixed points are observable as large time solutions, given appropriate initial conditions. In what follows we use numerically computed solutions from each of the windows which support multimodal steady states (i.e. 3M, 4M, 5M, 6M, 7M, 8M and 9M) and show that they come from the unimodal fixed point attractor in interval A (see Figure 1).

Making the assumption that the multimodal fixed points arise from the self-similar property (26), we first transform the  $\nu$ -windows which support these steady states by multiplying by  $N^2$  where  $N$  is the modal characterization of the attractor. This transformation gives the corresponding viscosity interval in the global fixed point attractor A of Figure 1. The results are summarized in Table 1.

Attractor	$\nu$ interval	Transformed $\nu$ -interval ( $\times N^2$ )
3M	[.07465,.059922]	[.67185,.539298]
4M	[.043848,.034625]	[.701568,.554]
5M	[.026984,.022604]	[.6746,.5651]
6M	[.01829,.015845]	[.65844,.57042]
7M	[.012994,.01174]	[.636706,.57526]
8M	[.009905,.009204]	[.63392,.589056]
9M	[.007479,.007305]	[.605799,.591705]
10M	.006	.6

Table 1

Table 1 indicates that the transformed intervals for each of the multimodal attractors listed lie in the  $\nu$ -interval which supports a unimodal global fixed point. In what follows we provide numerical evidence that each of the multimodal attractors at decreasing values of  $\nu$ , are indeed obtainable from the transformation (26). This is done for the profile corresponding to  $\nu = .6$  in interval A, since this is seen to be common to all entries in the Table. For  $N = 3, \dots, 10$  we compute the steady state attractor at the corresponding values  $\nu = 0.6/N^2$  and denote the profile by  $u_N(x)$ . These profiles are shown in Figure 14; the period of corresponding profiles is seen to be  $2\pi/N$  and the amplitude increases with  $N$ . Note that due to translation invariance each of the profiles can be shifted by a constant along the  $x$ -axis and it remains a periodic solution. This observation is particularly useful in the normalization construction that follows. Each profile is then *normalized* according to (26), that is we define a new function,  $U_N(y)$  say, on  $[0, 2\pi]$  by applying the transformation

$$U_N(y) = \frac{1}{N} u_N(x/N). \quad (25)$$

This transformation was first noted by Frisch et al. [12] who went on to carry out the linear stability of these profiles for large  $N$  - see below. If the self-similarity property (26) is valid for these multimodal fixed points, then the  $U_N(y)$  for  $N = 1, \dots, 10$  are identical to within a horizontal shift and equal to the profile obtained at  $\nu = 0.6$ . It was found that the computed profiles 4M-10M had to be shifted by  $\pi$  in order to put them in phase with the globally attracting profile at  $\nu = 0.6$  (see earlier comments). The results are given in Figure 15 with different symbols used to denote different values of  $N$ . The solid line corresponds to the generating fixed point at  $\nu = 0.6$ . It is seen from the Figure that the self-similarity property is indeed the controlling mechanism in the generation of these high-modal steady states as  $\nu$  decreases.

The data of Table 1 indicate the parameter range of the fixed point unimodal attractor which needs to be considered in order to transform, according to the similarity property, to the interval obtained numerically for a given multimodal attractor. In the stability studies of Frisch et al [12] and Papageorgiou et al [26], the underlying basic profiles are the multimodal ones indicated above and constructed in the Appendix, as the value of  $N$  or  $\rho$  increases. Such solutions are found to be stable in the  $\nu$ -interval (0.6, 0.7), approximately. This result would imply that given a value of  $\nu$  in the stability window, the multimodal profiles obtained by the self similarity property (26), i.e. the one-parameter family  $Nu(Nx; \nu/N^2)$  for  $N = 1, 2, \dots$  as  $N$  gets large, are linearly stable. Our numerical results are in agreement with this theoretical prediction for  $N$  as large as 10. Note that computation of steady states with  $N > 10$  has not been achieved yet because the window which supports such states has size of the order of machine precision. This may be achievable with higher precision arithmetic but such explorations are not undertaken here.

## 4 Conclusions

We have given many quantitative features of solutions of the Kuramoto-Sivashinsky equations computed with general initial data and spatially periodic boundary conditions. Features such as strange attractors and periodic or chaotic bursting phenomena have been elucidated. Of particular interest is a set of computed multimodal solutions found at decreasing values of  $\nu$  and supported on smaller and smaller windows. It has been shown that these solutions (the last computed one is a decamodal profile, i.e. one with all Fourier coefficients zero except those which are multiples of 10) derive from the unimodal fixed point attractor in  $.3 < \nu < 1$ , by a self-similar transformation property of the equation. It can be concluded that such solutions are at least linearly stable (in the sense that they are computable as large time solutions of a nonlinear initial value problem) and our numerical results are in full agreement with the stability theory of Frisch et al [12] and the modulation theory of Papageorgiou et al [26] who study the stability of such multimodal steady states. The numerical results given here provide strong support for the modulation stability theories.

## APPENDIX

The following property of (2) is useful. It has been established numerically that for  $0.307602 < \nu < 1$  (this is interval A described in Figure 1 and Section 3) the KS has a global unimodal fixed point attractor. That is given fairly general initial conditions (for example a white noise spectrum) solutions evolve to a steady state with period  $2\pi$ . Denote such steady states by  $U(x; \nu)$  with  $\nu$  in the interval A. For any constants  $\rho$  and  $c$ , equation (2) has the following two-parameter family of solutions

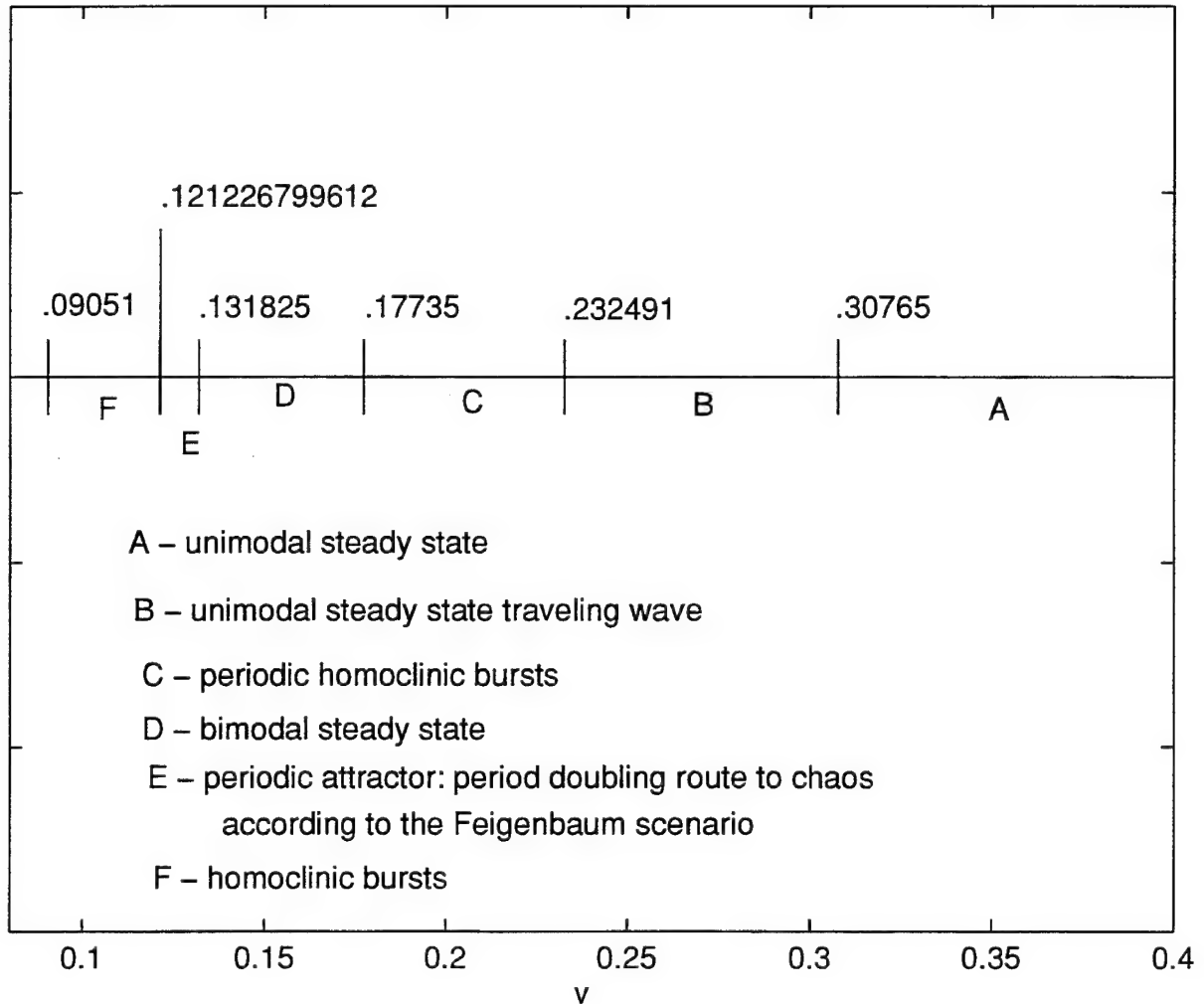
$$u(x, t) = \rho U(\rho(x - ct); \rho^2 \nu) + c. \quad (26)$$

This follows by the scale and Galilean invariance of KS. For stationary waves  $c = 0$ , while periodicity implies that  $\rho$  is an integer. Property (26) can be used to generate steady states of (2) at geometrically decreasing values of the viscosity. For example if the  $2\pi$ -periodic steady state is known at  $\nu = 0.8$ , we can construct a steady state at  $\nu = 0.8/2^2$  by choosing  $\rho = 2$ ; this solution has period  $\pi$ , i.e. is bimodal, and amplitude twice that of the starting steady state; this folding and scaling process can be repeated ad infinitum to obtain multimodal steady states at geometrically decreasing values of  $\nu$ . Clearly in the small  $\nu$  limit the amplitude of such steady states is of the order of  $\nu^{-1/2}$ , which is also the order of the  $L^2$ -norm of these steady state solutions. Even though the steady states exist and can be constructed as shown above, they are not necessarily stable and may not be observed in numerical experiments. What has been found, however, is that there is a subwindow of interval A which can be used to generate multimodal steady states which are linearly stable.

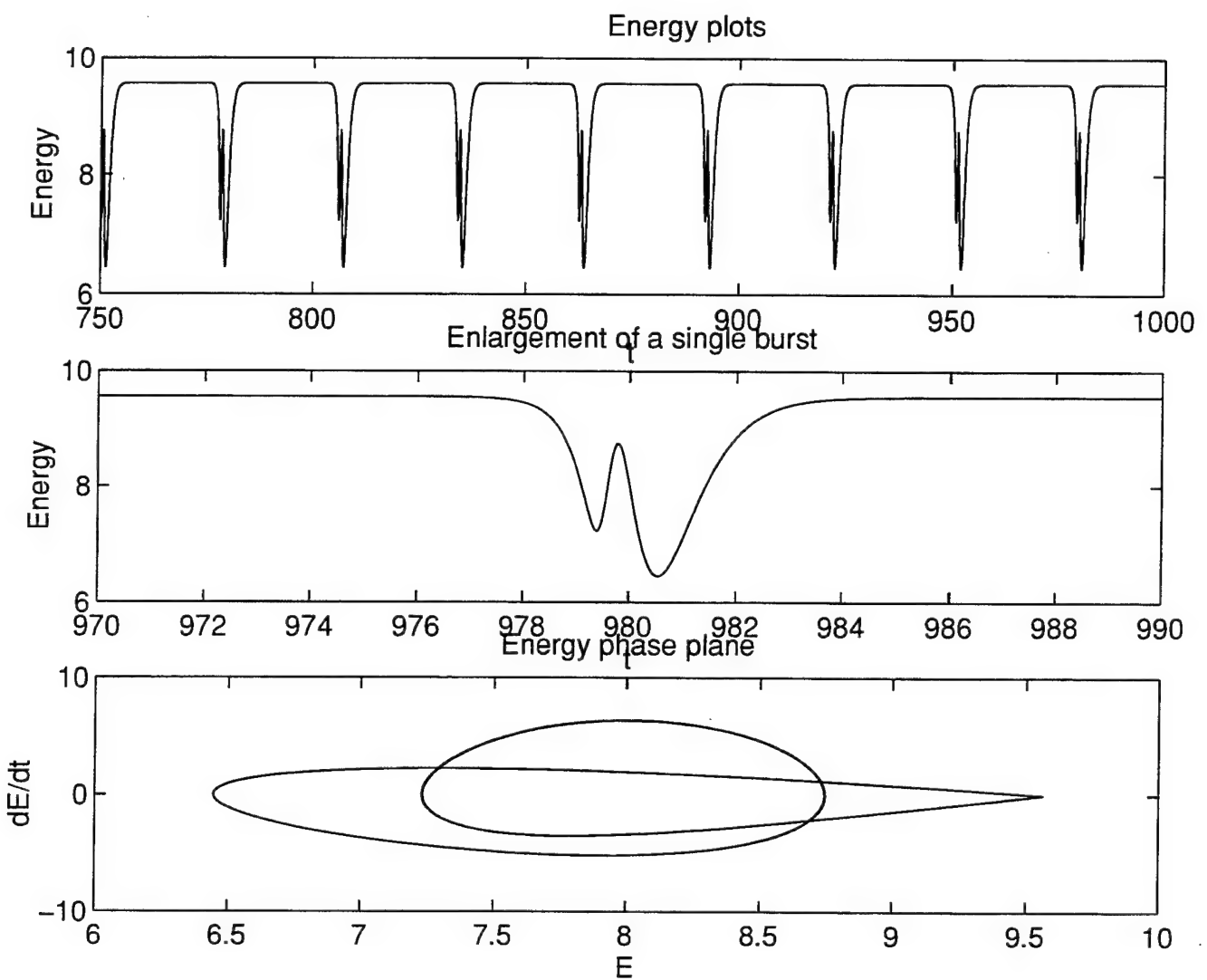
## References

- [1] Aimar, E.T., *Étude numérique d'une équation d'évolution nonlinéaire dérivant instabilité thermodiffusive d'un front de flame*, Thèse, Troisième cycle, Université de Provence (1982).
- [2] Benney, D.J., *Long Waves in Liquid films*, J. Math. and Phys. **45** (1966), pp. 150-155.
- [3] Chen, W., *Low dimensional approximate inertial manifolds for the Kuramoto-Sivashinsky equation*, Numer. Funct. Anal. and Optimiz., **14**(3&4) (1993), pp. 265-274.
- [4] Cohen, B.I., Krommes, J.A., Tang, W.M., Rosenbluth, M.N., *Non-linear saturation of the dissipative trapped ion mode by mode coupling*, Nucl. Fusion, **16**, (1976), pp. 971-992.
- [5] Collet, P., Eckmann, J.-P., Epstein, H., Stubbe, J., *A global attracting set for the Kuramoto-Sivashinsky equation*, Commun. Math. Phys., **152** (1993), pp. 203-214.
- [6] Collet, P., Eckmann, J.-P., Epstein, H., Stubbe, J., *Analyticity for the Kuramoto-Sivashinsky equation*, Physica D, **67** (1993), pp. 321-326.
- [7] Coward, A.V., Papageorgiou, D.T., Smyrlis, Y.S., *Nonlinear stability of oscillatory core-annular flow: A generalized Kuramoto-Sivashinsky equation with time periodic coefficients*, Zeit. Angew. Math. Phys. (ZAMP), **46** (1995), pp. 1-39.
- [8] Feigenbaum, M., *The onset of spectrum turbulence*, Phys. Lett. B, **74** (1979), pp. 375-378.
- [9] Feigenbaum, M., *The transition to aperiodic behavior in turbulent systems*, Commun. Math. Phys., **77** (1980), pp. 65-86.
- [10] Foias, C., Jolly, M.S., Kevrekidis, I.G., Titi, E.S., *On some dissipative fully discrete nonlinear Galerkin schemes for the Kuramoto-Sivashinsky equation*, Phys. Lett. A, **186** (1994), pp. 87-96.
- [11] Frenkel, A.L., Babchin, A.J., Levich, B.G., Shlang, T., Sivashinsky, G.I., J. Colloid. Interface Sci., **115** (1987), pp. 225.
- [12] Frisch, U., She, Z.S., Thual, O., *Viscoelastic behavior of cellular solutions of the Kuramoto-Sivashinsky equation*, J. Fluid Mech., **168** (1986), pp. 221-240.
- [13] Goodman, J., *Stability of the Kuramoto-Sivashinsky equation and related systems*, Comm. Pure Appl. Math., **XLVII** (1994), pp. 293-306.
- [14] Hooper, A.P., Grimshaw, R., *Nonlinear instability at the interface between two fluids*, Phys. Fluids, **28** (1985), pp. 37-45.
- [15] Hyman, J.M., Nicolaenko, B., *The Kuramoto-Sivashinsky equations, a bridge between PDEs and dynamical systems*, Physica D, **18** (1986), pp. 113-126.
- [16] Hyman, J.M., Nicolaenko, B., Zaleski, S., *Order and complexity in the Kuramoto-Sivashinsky model of turbulent interfaces*, Physica D, **23** (1986), pp. 265-292.
- [17] Il'yashenko, J.S., *Global analysis of the phase portrait for the Kuramoto-Sivashinsky equation*, J. Dyn. Diff. Equations, **4**(4) (1992), pp. 585-615.
- [18] Kevrekidis, I.G., Nicolaenko, B., Scovel, C., *Back in the saddle again: a computer assisted study of the Kuramoto-Sivashinsky equation*, SIAM J. Appl. Math., **50** (1990), pp. 760-790.

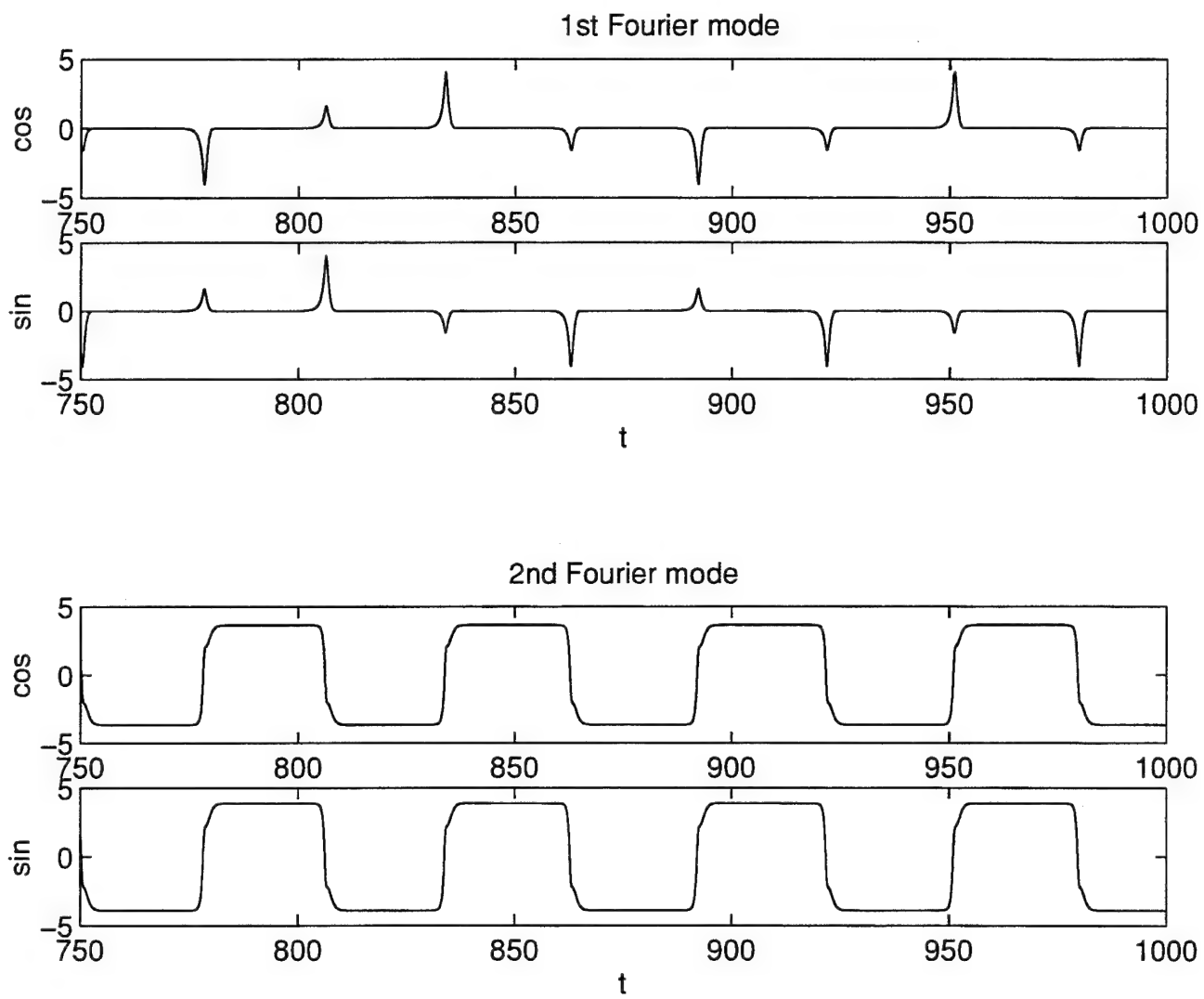
- [19] Kirby, M., *Minimal dynamical systems from PDEs using Sobolev eigenfunctions*, Physica D, **57** (1992), pp. 466-475.
- [20] Kuramoto, Y., *Diffusion induced chaos in reactions systems*, Progr. Theoret. Phys. Suppl., **64** (1978), pp. 346-367.
- [21] Kuramoto, Y., Tsuzuki, T., *On the formation of dissipative structures in reaction diffusion systems*, Progr. Theoret. Phys., **54** (1975), pp. 687-699.
- [22] Kuramoto, Y., Tsuzuki, T., *Persistent propagation of concentration waves in dissipative media far from thermal equilibrium*, Progr. Theoret. Phys., **55** (1976), pp. 356-369.
- [23] Manneville, P., *Lyapunov exponents for the Kuramoto-Sivashinsky equations*, Proc. Conf. on Turbulence, Nice 1984, Lecture Notes in Physics, Springer-Verlag, New York (1985).
- [24] Nicolaenko, B., Scheurer, B., Temam, R., *Some global dynamical properties of the Kuramoto-Sivashinsky equations: Nonlinear stability and attractors*, Physica D, **16** (1985), pp. 155-183.
- [25] Papageorgiou, D.T., Maldarelli, C., Rumschitzki, D.S., *Nonlinear interfacial stability of core-annular film flow*, Phys. Fluids A, **2**, No. 3 (1990), pp. 340-352.
- [26] Papageorgiou, D.T., Papanicolaou, G.C., Smyrlis, Y.S., *Modulational stability of periodic solutions of the Kuramoto-Sivashinsky equation*, ICASE Report No. 93-44 and SIAM J. Applied Math., submitted.
- [27] Papageorgiou, D.T., Smyrlis, Y.S. *The route to chaos for the Kuramoto-Sivashinsky equation*, Theoret. Comput. Fluid Dynamics, **3** (1991), pp. 15-42.
- [28] Robinson, J.C., *Inertial manifolds for the Kuramoto-Sivashinsky equation*, Phys. Lett. A, **184** (1994), pp. 190-193.
- [29] Shlang, T., Sivashinsky, G.I., *Irregular flow of a liquid film down a vertical column*, J. Phys., **43**, (1982), pp. 459-466.
- [30] Sivashinsky, G.I., *Nonlinear analysis of hydrodynamic instability in laminar flames, Part I. Derivation of basic equations*, Acta Astronautica, **4** (1977), pp. 1176-1206.
- [31] Sivashinsky, G.I., *On flame propagation under conditions of stoichiometry*, SIAM J. Appl. Math., **39** (1980), pp. 67-82.
- [32] Sivashinsky, G.I., Michelson, D.M., *On irregular wavy flow of a liquid down a vertical plane*, Prog. Theor. Phys. **63** (1980) 2112-2114.
- [33] Smyrlis, Y.S., Papageorgiou, D.T., *Predicting chaos for infinite-dimensional dynamical systems: The Kuramoto-Sivashinsky equation, a case study*, Proc. Nat. Acad. Sci. USA, **88** No. 24 (1991), pp. 11129-11132.
- [34] Temam, R., *Infinite dimensional dynamical systems in mechanics and physics*, Springer Verlag, New York (1988).
- [35] Tilley, B.S., Davis, S.H. and Bankoff, S.G. *Linear stability theory of two-layer flow in an inclined channel*, Phys. Fluids, **6** (1994), pp. 3906-3922.
- [36] Tilley, B.S., Davis, S.H. and Bankoff, S.G. *Nonlinear long-wave stability of superposed fluids in an inclined channel*, J. Fluid Mech., **277** (1994), pp. 55-83.



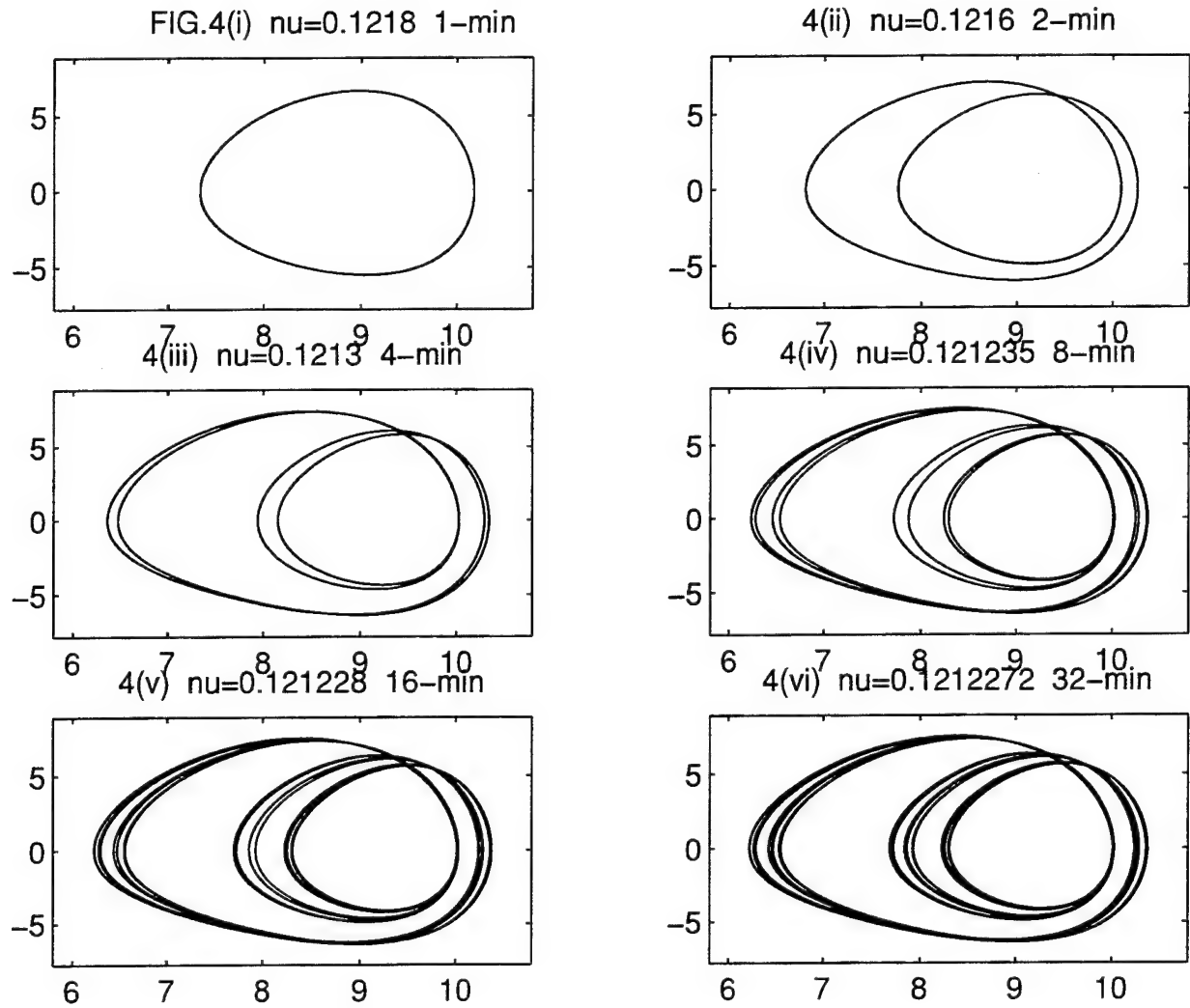
**Figure 1** Schematic of the various attractors for larger values of  $\nu$ . The diagram is to scale and the various most strongly attracting solution regions are indicated.



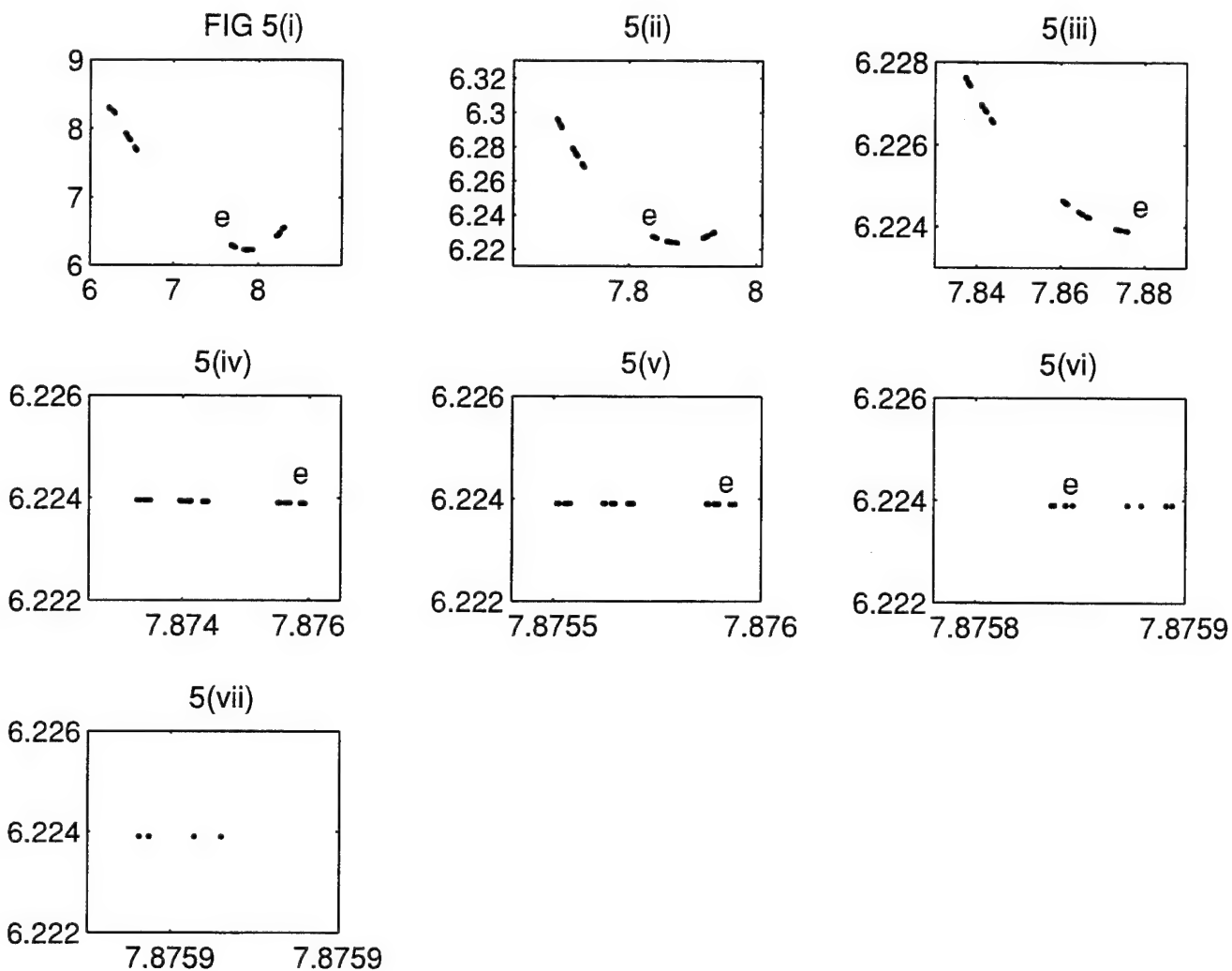
**Figure 2** Interval C: Periodic homoclinic bursts for  $\nu = 0.2$ . The energy and its phase plane are given.



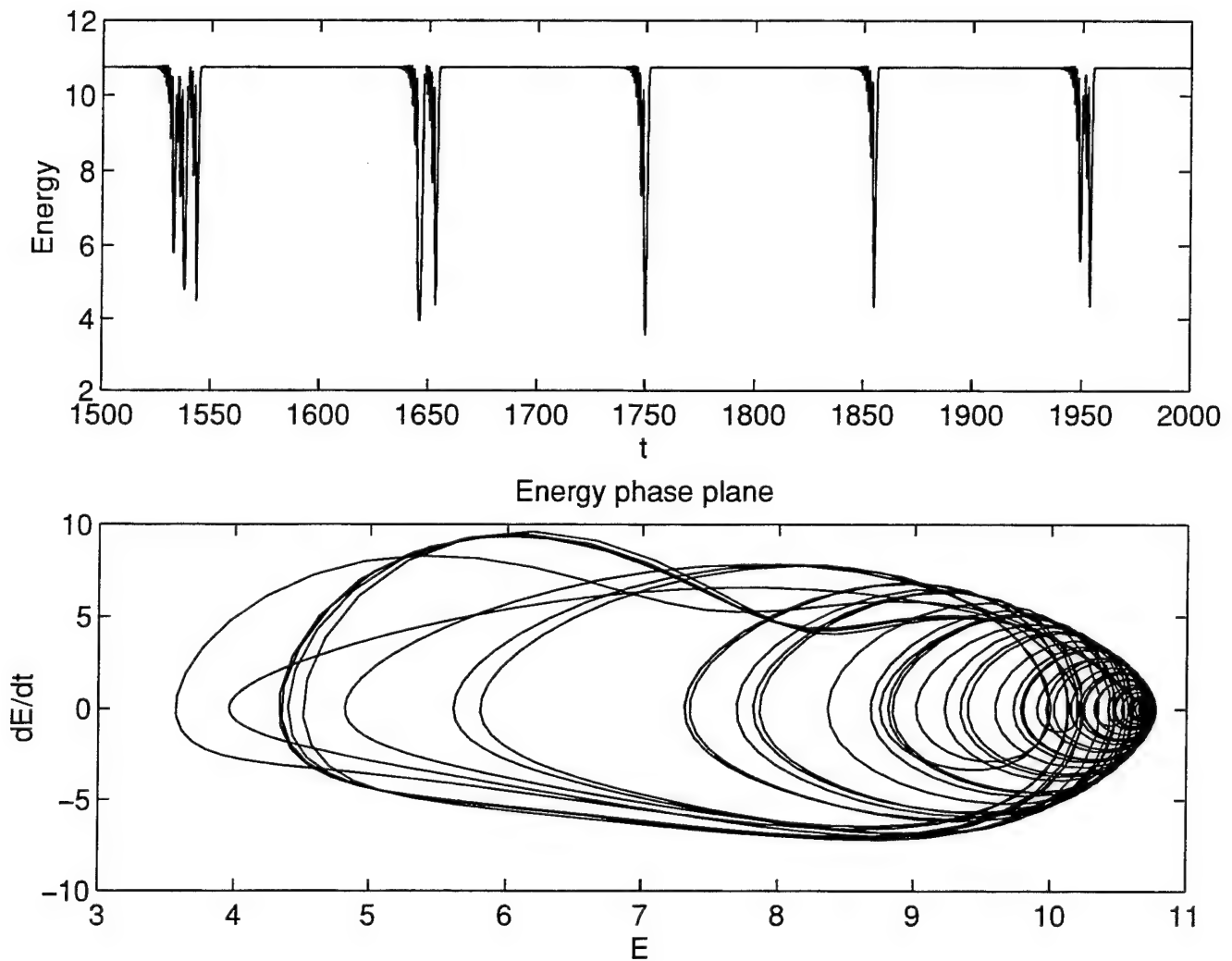
**Figure 3** Interval C: Periodic homoclinic bursts for  $\nu = 0.2$ . Time evolution of the 1st and 2nd Fourier modes. The graphs show the evolution of the coefficients of  $\cos(x), \sin(x)$  and  $\cos(2x), \sin(2x)$ . Higher mode amplitudes have much lower amplitudes.



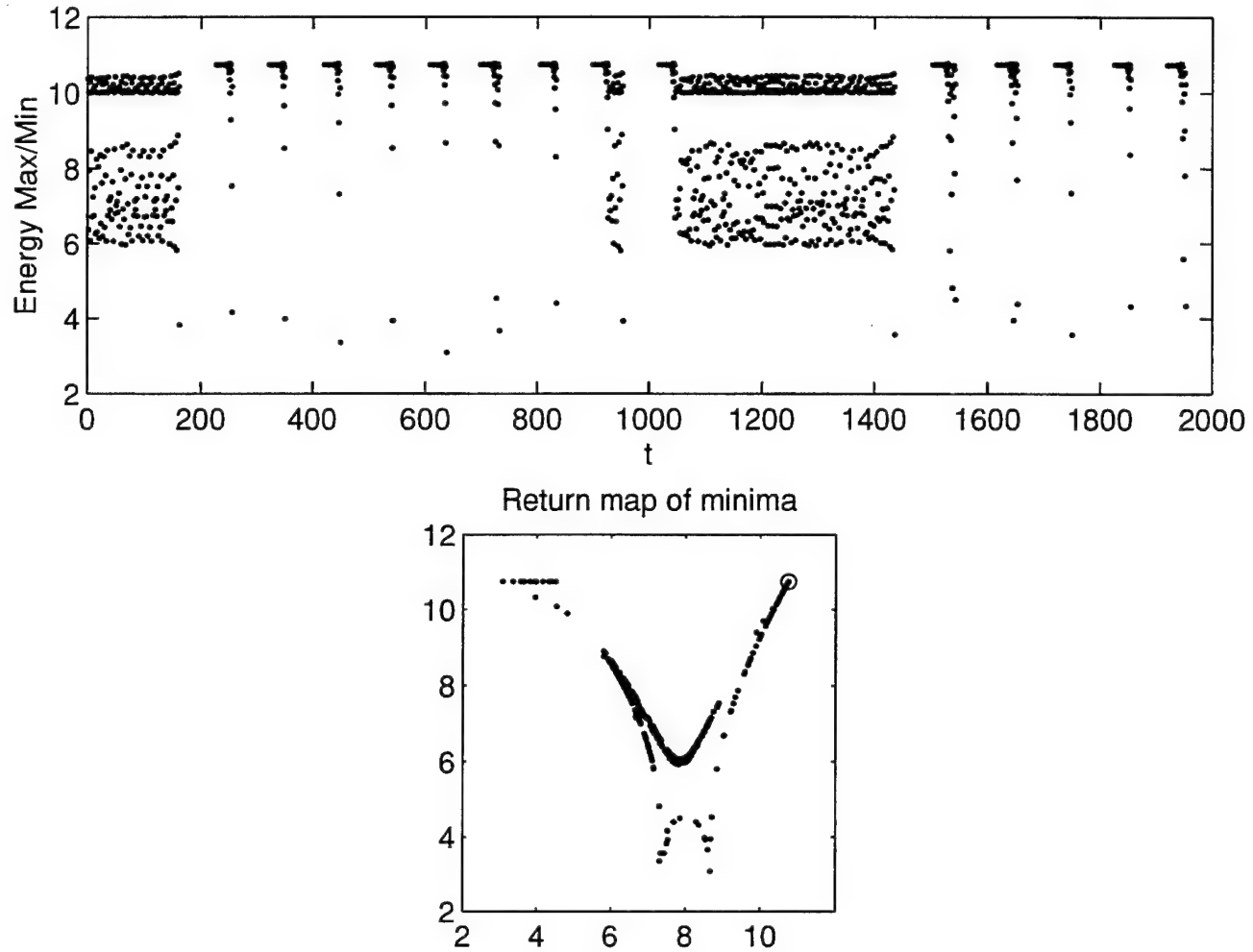
**Figure 4** Interval E: Period doubling route to chaos according to a Feigenbaum scenario. The Figure gives the phase planes of the energy as  $\nu$  decreases. The values of  $\nu$  and the number of relative minima in each curve are indicated on the Figure. Chaos sets in as the phase plane attains increasingly more turns which become infinitely many as an accumulation point is reached.



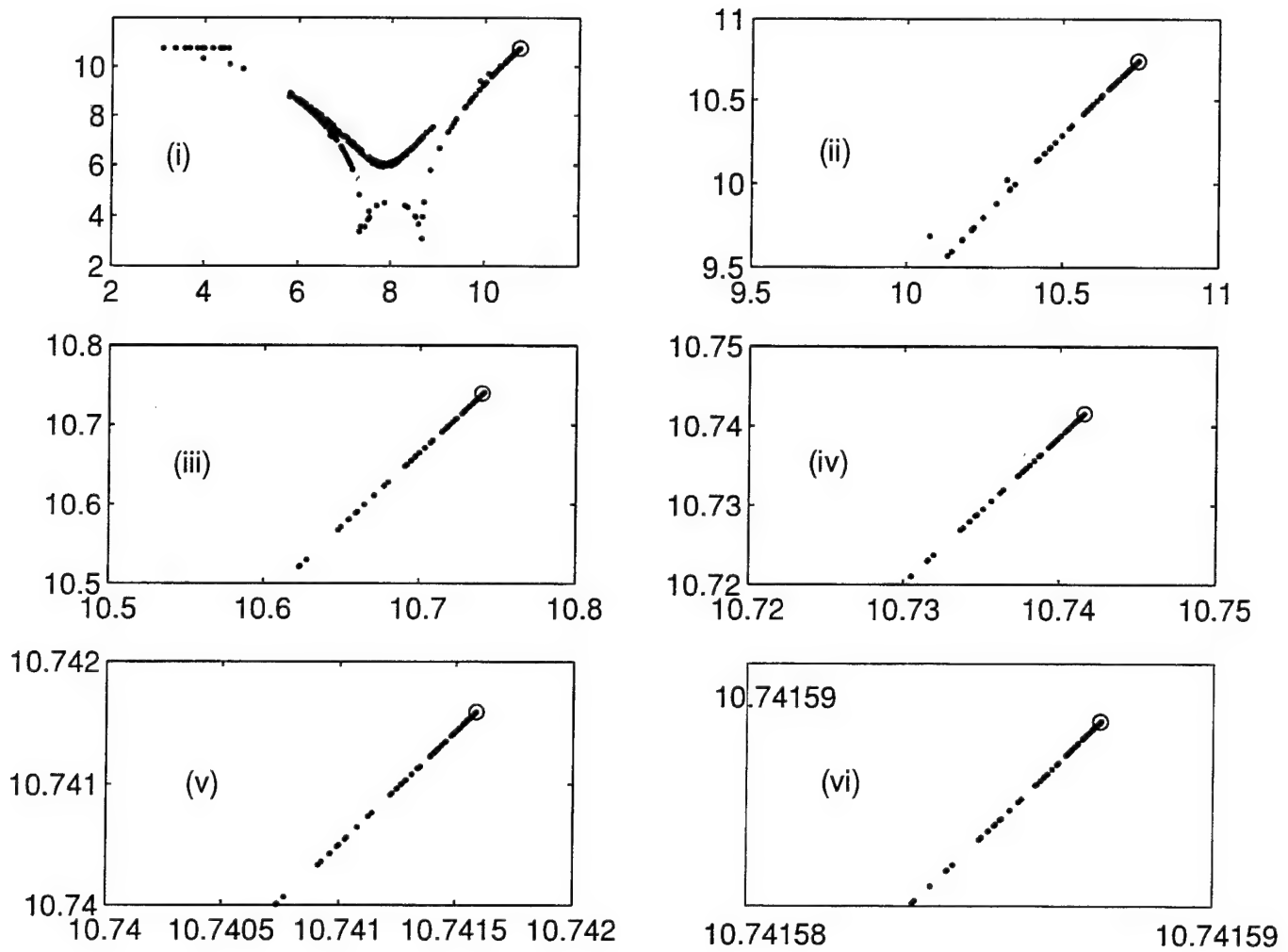
**Figure 5** Interval  $E_1$ : Feigenbaum chaos,  $\nu = 0.12118$ . Strange attractor produced by the return map of the energy minima. The Figure gives successive enlargements near the point 'e' marked on each subplot indicating the self-similar nature of the attractor. An overall enlargement of  $3 \times 10^6$  takes place in going from 5(i) to 5(vii).



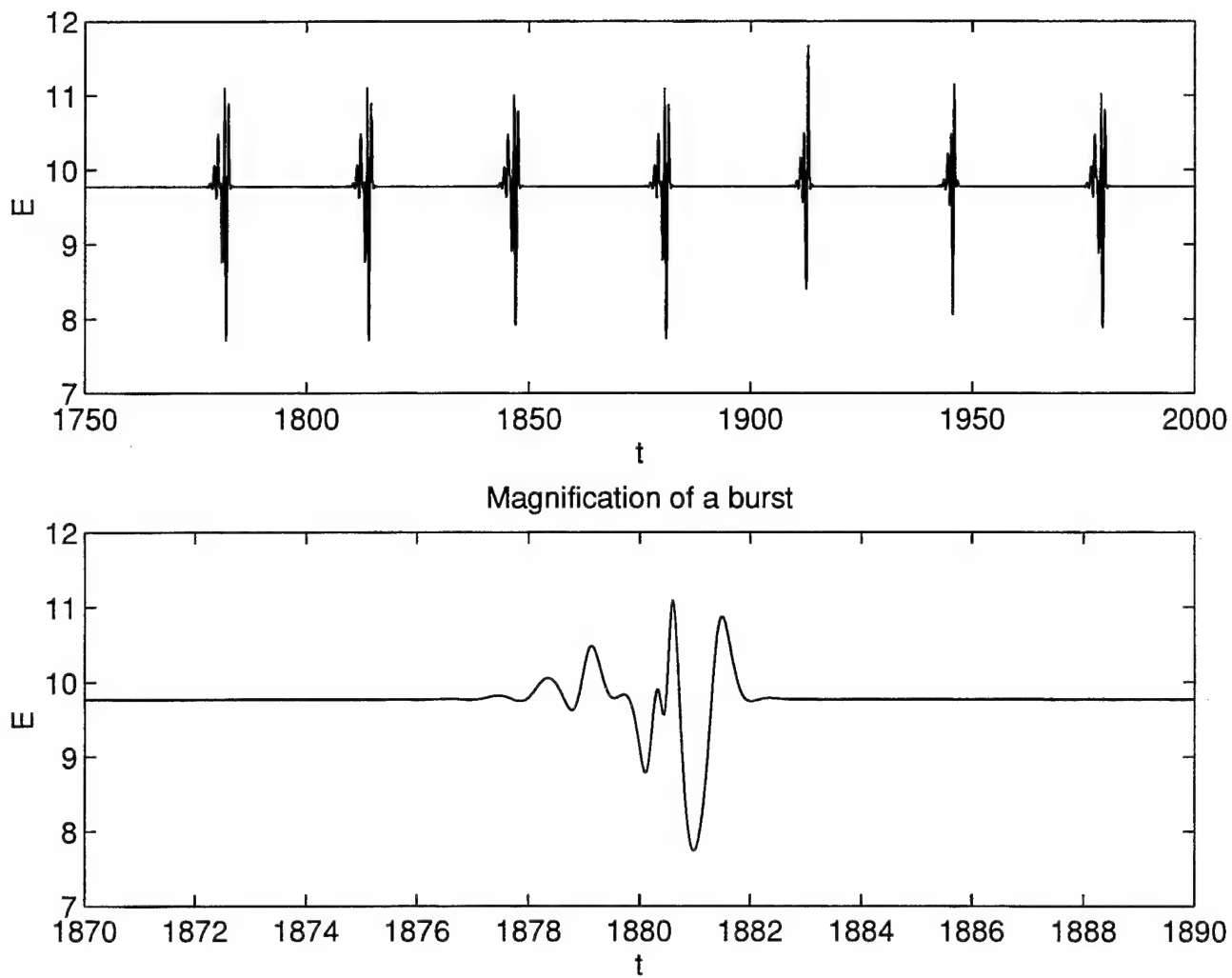
**Figure 6** Interval F: Chaotic homoclinic bursts,  $\nu = 0.12115$ . The energy and its phase plane are shown. The bursts occur at regular intervals and are chaotic in nature. The steady attractor between bursts corresponds to the unimodal global steady attractor in interval A having  $\nu = 0.4846$  and the similarity transformation (26) (see text).



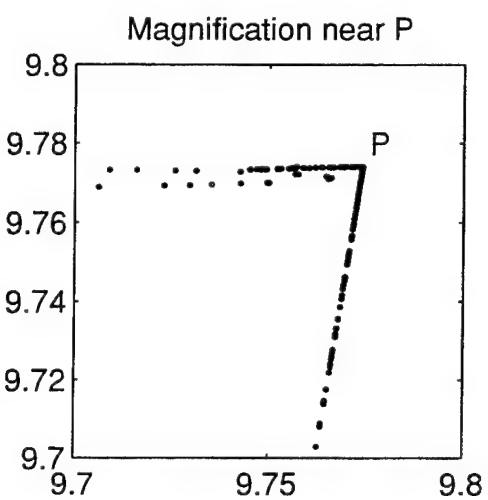
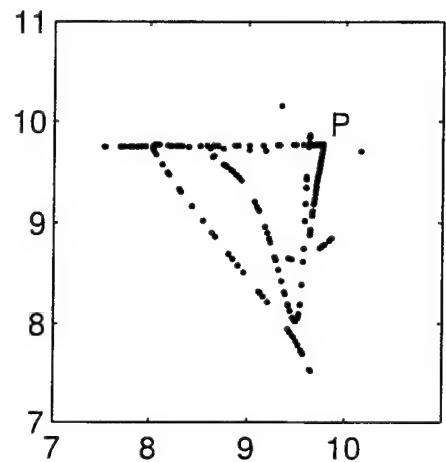
**Figure 7** Interval F: Chaotic homoclinic bursts,  $\nu = 0.12115$ . Time history of the critical points of the energy (both maxima and minima). The absence of points indicates a constant energy. An extended chaotic region is seen between approximately  $t = 1000 - 1400$ , which then gets attracted to chaotic homoclinic bursts. The lower figure shows the return map of the energy minima. A strange attractor emerges and the point between bursts is indicated by an open circle.



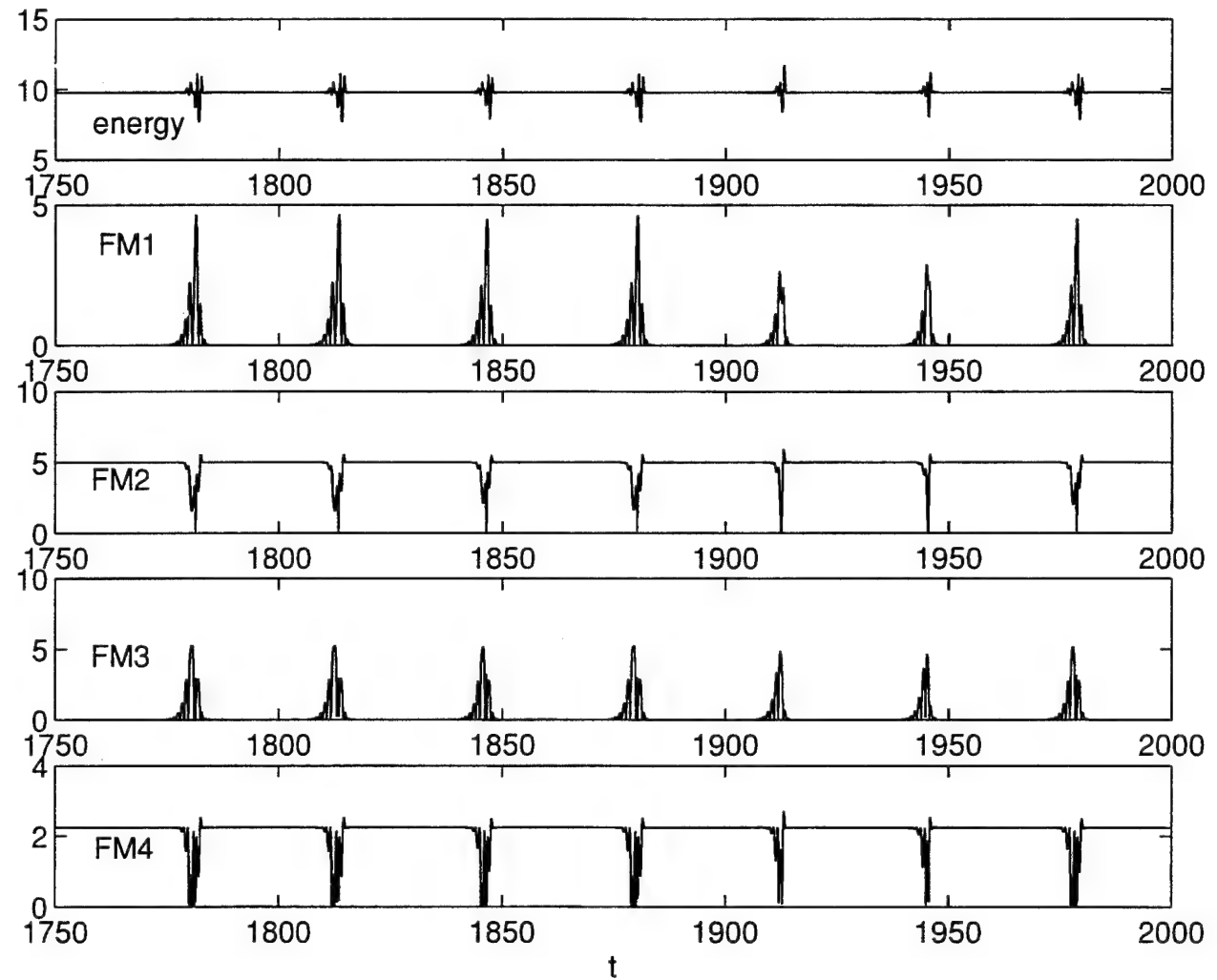
**Figure 8** Interval F: Chaotic homoclinic bursts,  $\nu = 0.12115$ . Self-similarity of the strange attractor. Successive enlargements are shown in the neighborhood of ‘o’. An overall enlargement of the order of  $10^5$  takes place in going from 8(i) to 8(vi).



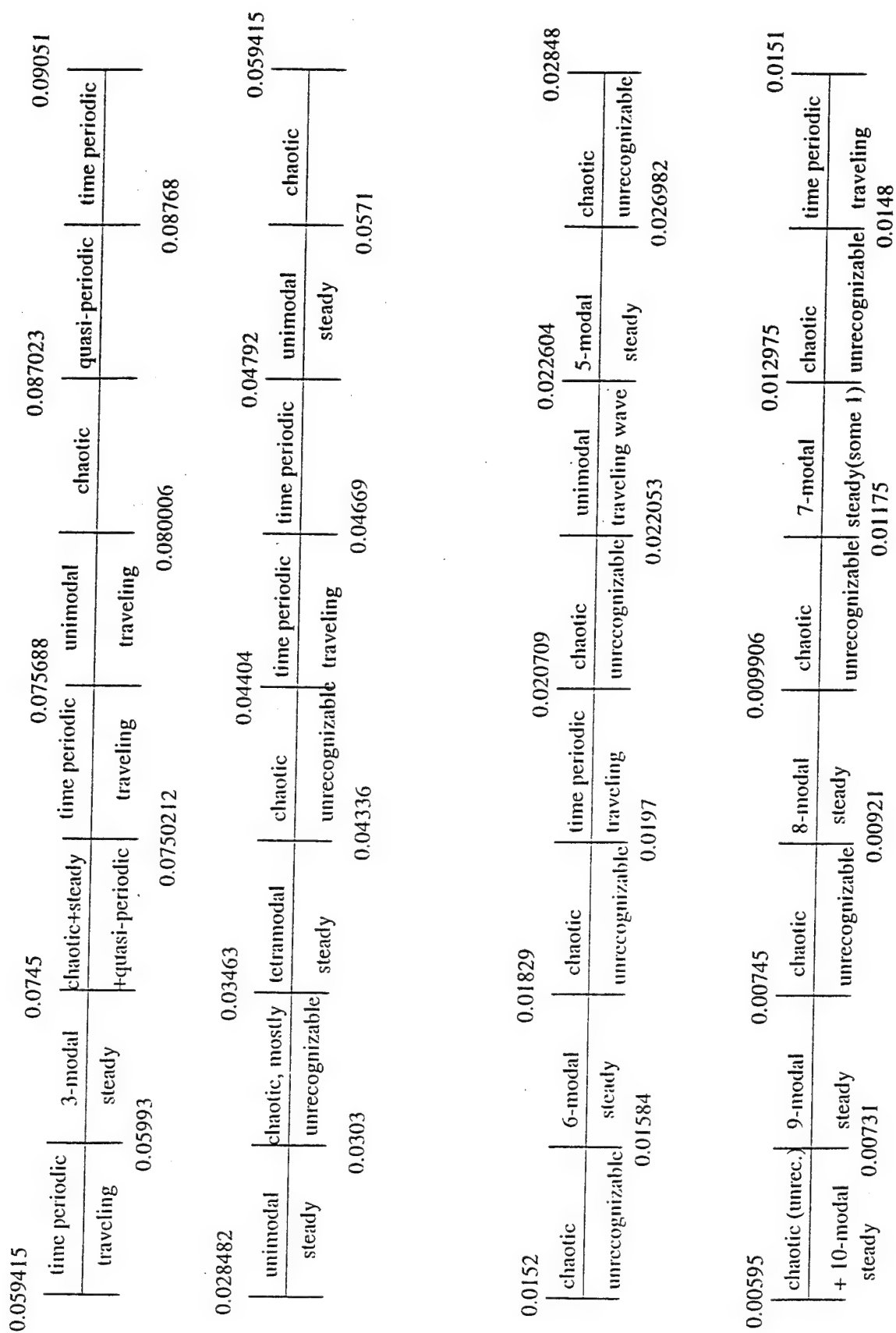
**Figure 9** Interval F: Chaotic homoclinic bursts,  $\nu = 0.1$ . Evolution of the energy together with an enlargement of a chaotic burst.

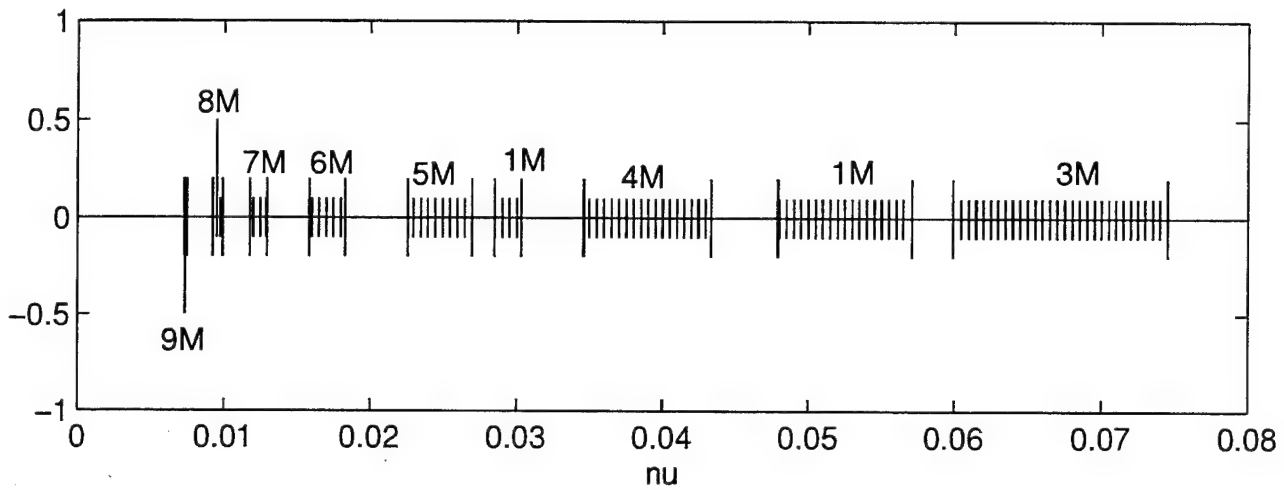


**Figure 10** Interval F: Chaotic homoclinic bursts,  $\nu = 0.1$ . Return map of the energy minima indicating a strange attractor. The point P indicates the position in between bursts.

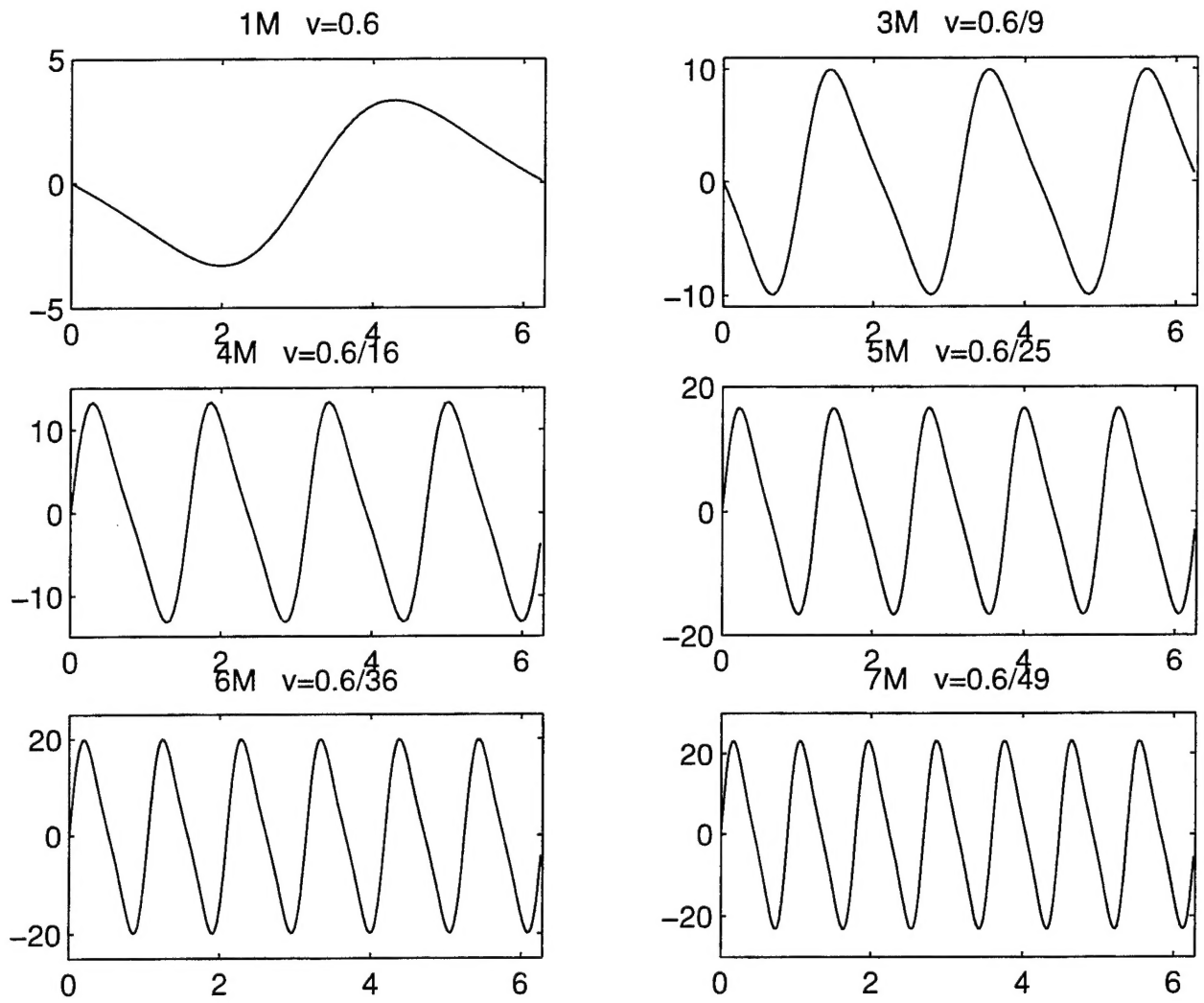


**Figure 11** Interval F: Chaotic homoclinic bursts,  $\nu = 0.1$ . Evolution of the first 4 Fourier amplitudes together with the energy (sum of the Fourier amplitudes). It is seen that in between bursts the even Fourier modes are non-zero while the odd ones are zero, and the steady attractor is bimodal, then. During bursting an energy exchange takes place with odd modes gaining energy from even modes. The interval between bursts remains fairly constant over long time periods.

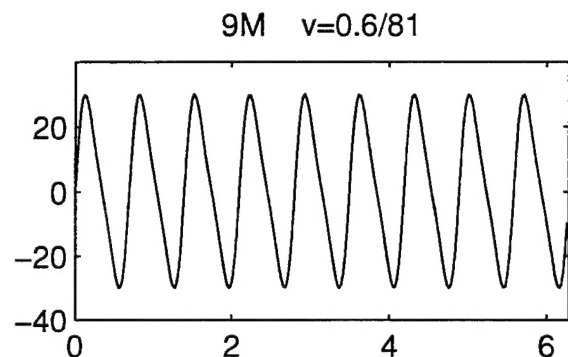
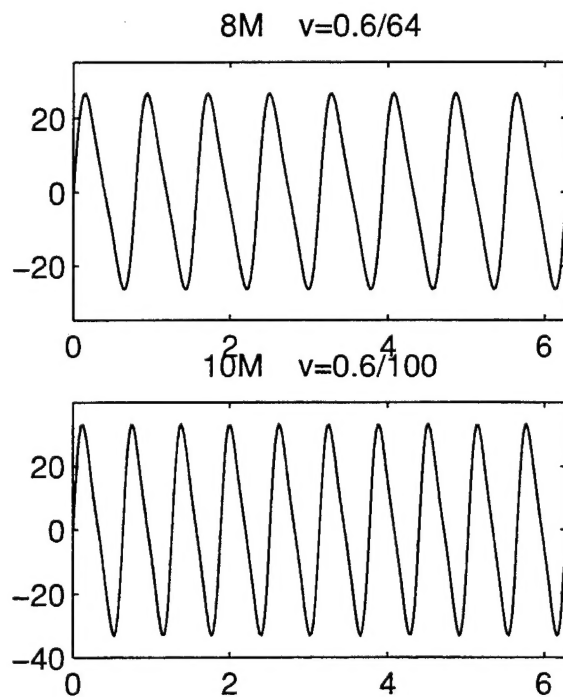




**Figure 13** Distribution of computed steady attractors for  $\nu < 0.09$ . The diagram, drawn to scale, shows the  $\nu$ -intervals where steady state solutions were found. The notation 1M, 3M, etc. denotes profiles which are unimodal, trimodal etc.. The windows of support of higher modal steady states get increasingly small as  $\nu$  decreases and their computation becomes prohibitively difficult.



**Figure 14** Computed profiles corresponding to values of  $\nu$  taken from the global attractor for large  $\nu$  (interval A in Figure 1) and the intervals 3M, 4M, 5M, 6M, 7M, 8M, 9M and 10M. The corresponding values of  $n\nu$  are indicated on the Figures and are chosen in order to check the self-similarity of the solutions (see text).



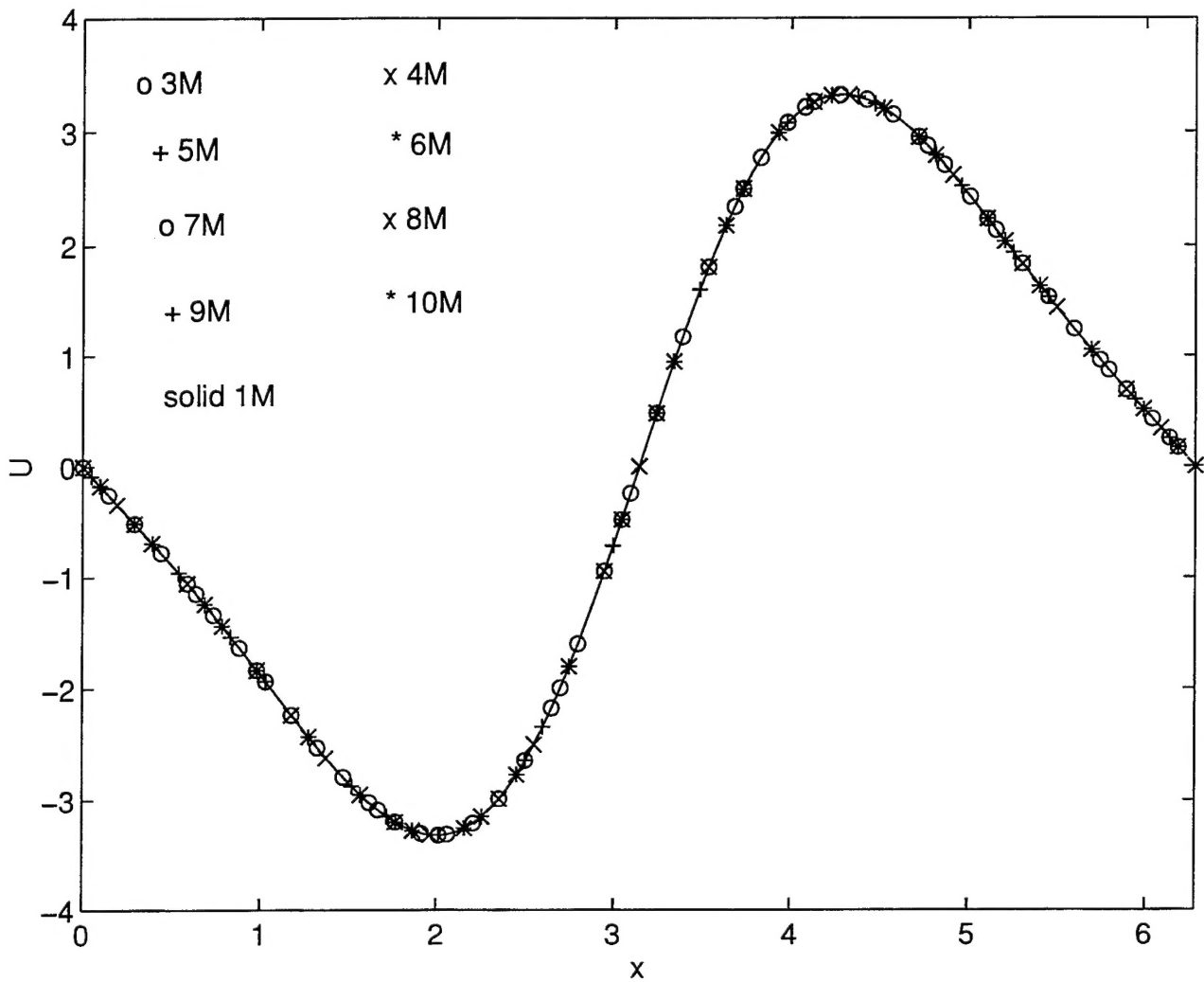


**Figure 15** Similarity of steady states as  $\nu$  decreases. Collapse of the profiles given in Figure 14 onto the universal profile corresponding to  $\nu = 0.6$ . Different symbols correspond to data taken from the indicated intervals. The similarity property (26) is used in the construction of the Figure - see text for details.

REPORT DOCUMENTATION PAGE			Form Approved OMB No. 0704-0188
<p>Public reporting burden for this collection of information is estimated to average 1 hour per response, including the time for reviewing instructions, searching existing data sources, gathering and maintaining the data needed, and completing and reviewing the collection of information. Send comments regarding this burden estimate or any other aspect of this collection of information, including suggestions for reducing this burden, to Washington Headquarters Services, Directorate for Information Operations and Reports, 1215 Jefferson Davis Highway, Suite 1204, Arlington, VA 22202-4302, and to the Office of Management and Budget, Paperwork Reduction Project (0704-0188), Washington, DC 20503.</p>			
1. AGENCY USE ONLY(Leave blank)	2. REPORT DATE	3. REPORT TYPE AND DATES COVERED	
	February 1996	Contractor Report	
4. TITLE AND SUBTITLE		5. FUNDING NUMBERS	
COMPUTATIONAL STUDY OF CHAOTIC AND ORDERED SOLUTIONS OF THE KURAMOTO-SIVASHINSKY EQUATION		C NAS1-19480 WU 505-90-52-01	
6. AUTHOR(S)			
Yiorgos S. Smyrlis Demetrios T. Papageorgiou			
7. PERFORMING ORGANIZATION NAME(S) AND ADDRESS(ES)		8. PERFORMING ORGANIZATION REPORT NUMBER	
Institute for Computer Applications in Science and Engineering Mail Stop 132C, NASA Langley Research Center Hampton, VA 23681-0001		ICASE Report No. 96-12	
9. SPONSORING/MONITORING AGENCY NAME(S) AND ADDRESS(ES)		10. SPONSORING/MONITORING AGENCY REPORT NUMBER	
National Aeronautics and Space Administration Langley Research Center Hampton, VA 23681-0001		NASA CR-198283 ICASE Report No. 96-12	
11. SUPPLEMENTARY NOTES			
Langley Technical Monitor: Dennis M. Bushnell Final Report To appear in Advances in Multi-Fluid Flows.			
12a. DISTRIBUTION/AVAILABILITY STATEMENT		12b. DISTRIBUTION CODE	
Unclassified-Unlimited  Subject Category 64			
13. ABSTRACT (Maximum 200 words)			
We report the results of extensive numerical experiments on the Kuramoto-Sivashinsky equation in the strongly chaotic regime as the viscosity parameter is decreased and increasingly more linearly unstable modes enter the dynamics. General initial conditions are used and evolving states do not assume odd-parity. A large number of numerical experiments are employed in order to obtain quantitative characteristics of the dynamics. We report on different routes to chaos and provide numerical evidence and construction of strange attractors with self-similar characteristics. As the "viscosity" parameter decreases the dynamics becomes increasingly more complicated and chaotic. In particular it is found that regular behavior in the form of steady state or steady state traveling waves is supported amidst the time-dependent and irregular motions. We show that multimodal steady states emerge and are supported on decreasing windows in parameter space. In addition we invoke a self-similarity property of the equation, to show that these profiles are obtainable from global fixed point attractors of the Kuramoto-Sivashinsky equation at much larger values of the viscosity.			
14. SUBJECT TERMS		15. NUMBER OF PAGES	
dissipative dynamical systems; chaotic solutions; coherent structures		34	
		16. PRICE CODE	
		A03	
17. SECURITY CLASSIFICATION OF REPORT	18. SECURITY CLASSIFICATION OF THIS PAGE	19. SECURITY CLASSIFICATION OF ABSTRACT	20. LIMITATION OF ABSTRACT
Unclassified	Unclassified		